

# Distances, Luminosities, and Temperatures of the Coldest Known Substellar Objects

Trent J. Dupuy<sup>1,2\*</sup> and Adam L. Kraus<sup>1,3</sup>

<sup>1</sup>Harvard-Smithsonian Center for Astrophysics, 60 Garden St, Cambridge, MA 02138, USA

<sup>2</sup>Hubble Fellow

<sup>3</sup>University of Texas at Austin, Astronomy Department, Austin, TX 78712, USA

\*To whom correspondence should be addressed; E-mail: [tdupuy@cfa.harvard.edu](mailto:tdupuy@cfa.harvard.edu).

**The coolest known brown dwarfs are our best analogs to extrasolar gas-giant planets. The prolific detections of such cold substellar objects in the past two years has spurred intensive followup, but the lack of accurate distances is a key gap in our understanding. We present a large sample of precise distances based on homogeneous mid-infrared astrometry that robustly establish absolute fluxes, luminosities, and temperatures. The coolest brown dwarfs have temperatures of 400–450 K and masses  $\approx 5\text{--}20\times$  that of Jupiter, showing they bridge the gap between hotter brown dwarfs and gas-giant planets. At these extremes, spectral energy distributions no longer follow a simple correspondence with temperature, suggesting an increasing role of other physical parameters such as surface gravity, vertical mixing, clouds, and metallicity.**

One major goal in astrophysics is to extend previous successes in the characterization and modeling of stellar atmospheres to the much cooler atmospheres of extrasolar planets. A key pathway is the identification of free-floating objects that not only share common temperatures

with exoplanets but that also share common masses and thus surface gravities. In recent years, searches for ever colder free-floating brown dwarfs—objects with masses below the hydrogen-fusing mass limit—have steadily pushed the census of the solar neighborhood to ever lower masses and finally perhaps into the planetary-mass regime ( $\lesssim 13$  Jupiter masses).

The detection of large samples of brown dwarfs at the beginning of the last decade ushered in two, now widely accepted, spectral types denoted by the letters “L” and “T” that extend the canonical OBAFGKM scheme for classifying stars that had stood untouched for nearly a century. Over the last two years, candidates for a “Y” spectral class have been uncovered in binary surveys (1, 2) and in all-sky imaging data from *WISE*, the *Wide-field Infrared Survey Explorer* (3). The primary criterion adopted to trigger this class has been the appearance of ammonia ( $\text{NH}_3$ ) absorption in near-infrared ( $1\text{--}2.5\ \mu\text{m}$ ) spectra.

Y dwarfs probe colder atmospheric physics than before, with putative effective temperatures as low as  $T_{\text{eff}} \sim 300\ \text{K}$  and masses of  $\approx 5\text{--}20$  Jupiter masses (3). If found orbiting a star, a Y dwarf would likely be considered a gas-giant planet. However, these estimated properties of Y dwarfs are speculative given the uncertainty in their temperatures, ages, and luminosities. Temperatures have only been estimated from model atmospheres that use incomplete molecular line lists and simple prescriptions for complex processes like nonequilibrium chemistry and condensate formation.

An independent approach for determining temperatures is to combine bolometric luminosities ( $L_{\text{bol}}$ ) with evolutionary model-predicted radii ( $R_{\star}$ ) and apply the Stefan–Boltzmann Law,  $T_{\text{eff}} \equiv (4\pi\sigma R_{\star}^2/L_{\text{bol}})^{-1/4}$ . Recent observations of transiting substellar objects generally support evolutionary model radius predictions over a wide range of masses (4–6). Although many may not be ideal test cases, since they may have formed via core accretion or have been intensely irradiated, variations in radii are expected to be relatively small and not strongly influence our resulting temperatures given the weak dependence on radius ( $T_{\text{eff}} \propto R_{\star}^{-1/2}$ ). Therefore, the

key measurements needed to determine temperatures via luminosity are accurate distances to Y dwarfs, along with a method for computing  $L_{\text{bol}}$  from multi-wavelength photometry.

Trigonometric parallaxes provide the only direct means of measuring distances to stars. A star’s distance is inversely proportional to the amplitude of its apparent periodic motion on the sky relative to more distant background stars, which is due to the Earth’s orbital motion around the Sun. The amplitude of this effect is small, 0.1 arcseconds for a star at 10 parsec, and thus measuring parallaxes requires long-term, precise position measurements. We have been using the Infrared Array Camera (IRAC) on board the *Spitzer Space Telescope* to obtain such astrometry of late-T and Y dwarfs from 2011–2012.

*Spitzer* currently trails the Earth by  $\approx 2$  months in its solar orbit, and keeping its solar shield directed at the Sun forces the telescope to observe stars near parallax maximum. By maintaining a cold temperature *Spitzer* can obtain sensitive images in the thermal mid-infrared, where Y dwarfs emit most of their flux, giving it an advantage over ground-based near-infrared observations of Y dwarfs. We also use an improved correction for the nonlinear optical distortion of *Spitzer/IRAC* that enables  $\sim 10\times$  smaller residual errors than the correction used by the standard data pipeline, allowing us to unlock the precision astrometric capabilities of *Spitzer*.

By combining our parallaxes (Table S1, Fig. S1) with photometry from the literature (7–9), we have determined absolute magnitudes in the near-infrared  $YJHK$  bands ( $\approx 1.0\text{--}2.4\ \mu\text{m}$ ) and *Spitzer*’s mid-infrared bands at  $3.6\ \mu\text{m}$  and  $4.5\ \mu\text{m}$  (Table S2, Fig. 1, Fig. 2). For each spectral type bin, we computed the weighted mean absolute magnitude as well as upper/lower limits on the amount of intrinsic scatter in the magnitudes (Table S3).

Objects classified as normal Y0 dwarfs are  $\approx 2$  magnitudes ( $\approx 6\times$ ) fainter in the near-infrared compared to the latest type T dwarfs, yet they generally share very similar colors. The most notable exception is that the  $Y - J$  colors become much bluer for Y dwarfs (9), which we find is due to flux at  $\approx 1.25\ \mu\text{m}$  dropping by  $5\times$  while flux at  $\approx 1.05\ \mu\text{m}$  only drops

by  $2.5\times$ . This behavior is consistent with prior speculation that Y dwarfs may be so cool that the alkali atoms that dominate absorption at blue wavelengths for warmer brown dwarfs finally become locked into molecules like  $\text{Na}_2\text{S}$  and  $\text{KCl}$ , thereby reducing the opacity at  $1.05\ \mu\text{m}$  relative to  $1.25\ \mu\text{m}$  (10). The appearance of such molecules could result in the return of substantial condensate clouds (11) and corresponding variability/weather.

In contrast to their near-infrared behavior, Y dwarfs show remarkable diversity in their mid-infrared colors. Even though they are only  $\approx 2\times$  fainter than the latest T dwarfs at these wavelengths, they range from the same color as late-T dwarfs to much redder ( $\approx 0.8$  magnitudes). One of the reddest objects is WISEP J1405+5534, which has been typed as “Y0 peculiar?” because its  $H$ -band spectral peak is shifted  $60\ \text{\AA}$  redder than the Y0 standard WISEP J1738+2732 (3). We find that WISEP J1405+5534 in fact has a very similar temperature to other Y0 dwarfs (Table S5) indicating that its unusual spectrum is due to another physical property. Both the mid-infrared color and peculiar spectrum may be explained by a reduced level of nonequilibrium chemistry in the photosphere, perhaps due to reduced vertical mixing. This would produce enhanced  $\text{NH}_3$  absorption at  $H$ -band as compared to other Y0 dwarfs and enhanced  $\text{CH}_4$  absorption relative to CO driving WISEP J1405+5534 to redder  $[3.6] - [4.5]$  colors.

The coldest brown dwarfs also demonstrate unusual behavior in their absolute fluxes as a function of spectral type. Despite the plummeting near-infrared flux—normal Y0 dwarfs are  $\approx 6\times$  fainter than the latest T dwarfs—Y0 dwarfs have indistinguishable fluxes compared to each other to within 15%–25%. This is very unusual compared to warmer brown dwarfs, which do not show such step-function behavior at any spectral type transition and also show much larger intrinsic scatter ( $\approx 30\%$ – $50\%$ ) in absolute fluxes for a given spectral type (12). This homogeneity among the Y0 dwarfs is further unexpected because it reverses the trend observed for the late-T dwarfs that the scatter increases substantially with later type, cooler objects (Fig. 3). For example, here we double the sample of T9 dwarfs with accurate distances

and find that their near-infrared fluxes typically have a scatter of 130%–210%.

Another unexpected result is that T9.5 dwarfs appear to be brighter at all bandpasses than the mean for T9 dwarfs and the T9 standard UGPS J0722–0540. Given the smaller sample of T9.5 dwarfs (three objects) and their more uncertain distances, this brightening is currently a  $2\sigma$  result, i.e., the weighted means in Table S3 are consistent with being equal at a  $p$ -value of 0.05. Such a brightening is reminiscent of the change in near-infrared fluxes from late-L to early-T dwarfs (13, 14), however we note that the brightening at the L/T transition only occurs at blue near-infrared wavelengths whereas we see brightening at all bands for the T9.5 dwarfs.

To derive bolometric luminosities from the absolute fluxes, we computed “super-magnitudes” by summing the fluxes in near- and mid-infrared bandpasses. This is an approximation to the standard method of integrating the observed spectral energy distribution as a function of wavelength, which is not possible for Y dwarfs given the current lack of sensitive mid-infrared spectrographs. We derived a multiplicative correction to account for the remaining flux not captured in these bands from a large grid of model atmospheres (11, 15). The weak dependence on these models is highlighted by the 8% fractional uncertainty in this correction factor (Fig. S4).

We used the Cond evolutionary models (16) to estimate radii and thereby temperatures, masses, and surface gravities from the bolometric luminosities of our sample (Fig. 4, Table S5). We assumed fiducial ages of 1 Gyr and 5 Gyr as expected for the field population (17, 18). The tangential velocities for our sample are consistent with having such typical ages. We find that the fractional change in temperature over this narrow range of spectral types is remarkably large: the mean temperature of T8 dwarfs is 685–745 K (for 1–5 Gyr), and this drops to 410–440 K for Y0 dwarfs (Table S6). Thus, these two subtypes alone span the same fractional range in temperature as the entire sequence of FGK stars (7300–4400 K) that are  $\sim 10\times$  hotter.

Although much cooler than their late-T counterparts, Y0 dwarfs turn out to be significantly warmer than previously suggested from model atmosphere fitting (Fig. S5). The most common

best-fit models of Y0 dwarfs in previous work have  $T_{\text{eff}} = 350$  K, with plausible model fits of 400 K in some cases (3). Thus, model fits are typically 60–90 K ( $\approx 15\%$ – $25\%$ ) cooler than we find from our distances combined with evolutionary model radii. If the fault lies with our assumed radii, they would need to be 30%–50% larger than expected because  $T_{\text{eff}} \propto R_{\star}^{-1/2}$ . This would require very young ages ( $\lesssim 100$  Myr) or very large systematic errors in the evolutionary models that are not likely given the aforementioned empirical validation from transiting brown dwarfs. Rather, we suggest that parameters derived from fitting model atmospheres to near-infrared spectra, where  $\lesssim 5\%$  of the flux emerges, are less likely to be accurate because current atmospheres imperfectly reproduce observed spectra.

Using our luminosity measurements, we find that the coldest brown dwarfs would be 6–10 Jupiter masses given an age of 1 Gyr. An older age of 5 Gyr implies 16–25 Jupiter masses. These masses therefore straddle the current demarcation of “planetary mass” set by the deuterium-fusing mass limit of  $\approx 13$  Jupiter masses (19–21). Thus, it is possible that the atmospheres of our objects harbor deuterated molecules such as HDO or CH<sub>3</sub>D that have not yet been detected because of the observational challenges (22).

Given the interest in both identifying the coldest atmospheric benchmarks and searching for the bottom of the initial mass function we briefly consider the most extreme objects in our sample in terms of temperature and mass. WISEP J1828+2650 has been dubbed the archetypal Y dwarf with a model-atmosphere temperature of  $\lesssim 300$  K, i.e., room temperature, based on extremely red colors implying that the Wien tail of its underlying blackbody distribution has moved into the near-infrared (3). Our luminosity for this object is inconsistent with such a low temperature, and we find it must be at least 420 K at  $2\sigma$ ; our calculations give  $520_{-50}^{+60}$  K at an age of 1 Gyr. (If WISEP J1828+2650 is a binary as proposed by (9) the  $2\sigma$  limit at 1 Gyr only drops to 360 K and 340 K for the hypothetical two components.) Its atypical properties compared to other Y dwarfs may simply be due to a slightly lower surface gravity, i.e., slightly younger age,

which qualitatively agrees with model predictions that the collapse in near-infrared flux happens at warmer temperatures for lower surface gravity (23). Ross 458C is a contender for the lowest mass object, at 7 Jupiter masses, if its age is near the 150 Myr lower limit of its proposed age range (24). However, WD 0806–661B is the most secure case for both lowest temperature (330–375 K) and lowest mass (6–10 Jupiter masses) object known, given that it has a precise age of  $2.0 \pm 0.5$  Gyr (25).

Overall, our results strengthen the connection between the coolest brown dwarfs and gas-giant exoplanets. We validate that they probe an extreme physical regime that bridges the gap between previously known, hotter brown dwarfs and Jupiter-like planets. We find that objects of very similar temperatures can have widely varying spectral energy distributions and absorption features, e.g., a range of 0.8 magnitudes in mid-IR colors for the same  $T_{\text{eff}}$ . Along with the fact that the  $\geq$ Y2 dwarf is warmer than the Y0 dwarfs, this implies that temperature is not the principal determinant in shaping spectra but rather seems to be on comparable footing with other physical properties such as surface gravity, vertical mixing, clouds, and perhaps metallicity. Consequently, the current spectral classification scheme used to identify Y dwarfs may not strongly correlate with temperature as it generally does for L and T dwarfs. This could explain the unusually homogeneous fluxes for Y0 dwarfs, unusually heterogeneous fluxes for T9 dwarfs, and plateau or brightening of flux from T9 to T9.5.

## References

1. K. L. Luhman, A. J. Burgasser, J. J. Bochanski, *ApJL* **730**, L9 (2011).
2. M. C. Liu, *et al.*, *ApJ* **740**, 108 (2011).
3. M. C. Cushing, *et al.*, *ApJ* **743**, 50 (2011).
4. M. Deleuil, *et al.*, *A&A* **491**, 889 (2008).

5. C. Hellier, *et al.*, *Nature* **460**, 1098 (2009).
6. D. R. Anderson, *et al.*, *ApJL* **726**, L19 (2011).
7. J. D. Kirkpatrick, *et al.*, *ApJS* **197**, 19 (2011).
8. J. D. Kirkpatrick, *et al.*, *ApJ* **753**, 156 (2012).
9. S. K. Leggett, *et al.*, *ApJ* **763**, 130 (2013).
10. M. C. Liu, T. J. Dupuy, B. P. Bowler, S. K. Leggett, W. M. J. Best, *ApJ* **758**, 57 (2012).
11. C. V. Morley, *et al.*, *ApJ* **756**, 172 (2012).
12. T. J. Dupuy, M. C. Liu, *ApJS* **201**, 19 (2012).
13. A. J. Burgasser, *et al.*, *ApJS* **166**, 585 (2006).
14. M. C. Liu, *et al.*, *ApJ* **647**, 1393 (2006).
15. D. Saumon, M. S. Marley, M. Abel, L. Frommhold, R. S. Freedman, *ApJ* **750**, 74 (2012).
16. I. Baraffe, G. Chabrier, T. S. Barman, F. Allard, P. H. Hauschildt, *A&A* **402**, 701 (2003).
17. A. J. Burgasser, *ApJS* **155**, 191 (2004).
18. P. R. Allen, D. W. Koerner, I. N. Reid, D. E. Trilling, *ApJ* **625**, 385 (2005).
19. D. Saumon, *et al.*, *ApJ* **460**, 993 (1996).
20. G. Chabrier, I. Baraffe, *ARA&A* **38**, 337 (2000).
21. P. Mollière, C. Mordasini, *A&A* **547**, A105 (2012).
22. G. Chabrier, I. Baraffe, F. Allard, P. Hauschildt, *ApJL* **542**, L119 (2000).



23. A. Burrows, D. Sudarsky, J. I. Lunine, *ApJ* **596**, 587 (2003).
24. A. J. Burgasser, *et al.*, *ApJ* **725**, 1405 (2010).
25. K. L. Luhman, *et al.*, *ApJ* **744**, 135 (2012).
26. G. G. Fazio, *et al.*, *ApJS* **154**, 10 (2004).
27. P. B. Stetson, *PASP* **99**, 191 (1987).
28. E. L. Wright, *et al.*, *AJ* **140**, 1868 (2010).
29. C. B. Markwardt, *Astronomical Society of the Pacific Conference Series*, D. A. Bohlender, D. Durand, & P. Dowler, ed. (2009), vol. 411, p. 251.
30. A. C. Robin, C. Reyl , S. Derri re, S. Picaud, *A&A* **409**, 523 (2003).
31. J. K. Faherty, *et al.*, *ApJ* **752**, 56 (2012).
32. S. K. Leggett, *et al.*, *ApJ* **748**, 74 (2012).
33. M. C. Liu, *et al.*, *ApJL* **740**, L32 (2011).
34. F. van Leeuwen, *A&A* **474**, 653 (2007).
35. K. A. Marsh, *et al.*, *ApJ* **762**, 119 (2013).
36. C. Beichman, *et al.*, *ApJ* **764**, 101 (2013).
37. T. E. Lutz, D. H. Kelker, *PASP* **85**, 573 (1973).
38. J. R. Thorstensen, *AJ* **126**, 3017 (2003).
39. D. Saumon, *et al.*, *ApJ* **656**, 1136 (2007).

40. A. J. Burgasser, *et al.*, *ApJL* **689**, L53 (2008).
41. G. Chabrier, I. Baraffe, F. Allard, P. Hauschildt, *ApJ* **542**, 464 (2000).
42. B. Tingley, *et al.*, *A&A* **528**, A97 (2011).
43. R. J. Siverd, *et al.*, *ApJ* **761**, 123 (2012).
44. J. A. Johnson, *et al.*, *ApJ* **730**, 79 (2011).
45. D. Saumon, M. S. Marley, *ApJ* **689**, 1327 (2008).
46. B. Burningham, *et al.*, *MNRAS* **395**, 1237 (2009).
47. D. J. Pinfield, *et al.*, *MNRAS* **422**, 1922 (2012).
48. E. L. Wright, *et al.*, *AJ* **145**, 84 (2013).
49. J. K. Faherty, *et al.*, *AJ* **137**, 1 (2009).
50. B. Burningham, *et al.*, *MNRAS* **433**, 457 (2013).
51. A. J. Burgasser, *et al.*, *ApJ* **586**, 512 (2003).
52. M. C. Liu, T. J. Dupuy, S. K. Leggett, *ApJ* **722**, 311 (2010).
53. C. G. Tinney, *et al.*, *ApJ* **759**, 60 (2012).
54. A. J. Burgasser, T. R. Geballe, S. K. Leggett, J. D. Kirkpatrick, D. A. Golimowski, *ApJ* **637**, 1067 (2006).
55. A. J. Burgasser, C. R. Gelino, M. C. Cushing, J. D. Kirkpatrick, *ApJ* **745**, 26 (2012).
56. B. Burningham, *et al.*, *MNRAS* **391**, 320 (2008).

57. B. Burningham, *et al.*, *MNRAS* **414**, 3590 (2011).
58. P. Delorme, *et al.*, *A&A* **482**, 961 (2008).
59. G. R. Knapp, *et al.*, *AJ* **127**, 3553 (2004).
60. S. K. Leggett, *et al.*, *ApJ* **695**, 1517 (2009).
61. S. K. Leggett, *et al.*, *ApJ* **710**, 1627 (2010).
62. D. L.Looper, J. D. Kirkpatrick, A. J. Burgasser, *AJ* **134**, 1162 (2007).
63. P. W. Lucas, *et al.*, *MNRAS* **408**, L56 (2010).
64. B. M. Patten, *et al.*, *ApJ* **651**, 502 (2006).
65. J. P. Subasavage, *et al.*, *AJ* **137**, 4547 (2009).
66. C. G. Tinney, A. J. Burgasser, J. D. Kirkpatrick, *AJ* **126**, 975 (2003).
67. W. F. van Altena, J. T. Lee, E. D. Hoffleit, *The General Catalogue of Trigonometric Stellar Parallaxes*, 4th ed., Yale University Observatory (1995).
68. S. J. Warren, *et al.*, *MNRAS* **381**, 1400 (2007).

We thank M. C. Liu for many helpful suggestions for improving this article; C. V. Morley for fruitful discussions regarding her and collaborators' model atmospheres, particularly the Vega zero points; M. C. Cushing for making available published spectra of our targets; and K. N. Allers for assistance in computing photometry from our IRAC data. This work is based on observations made with the *Spitzer Space Telescope*, which is operated by the Jet Propulsion Laboratory, California Institute of Technology under a

contract with NASA. T.J.D. acknowledges support from Hubble Fellowship grant HST-HF-51271.01-A awarded by the Space Telescope Science Institute, which is operated by AURA for NASA, under contract NAS 5-26555. A.L.K. was supported by a Clay Fellowship. Our imaging data are available in the *Spitzer* Heritage Archive at <http://sha.ipac.caltech.edu/applications/Spitzer/SHA>, and the astrometric measurements we derived are given in Table S1.

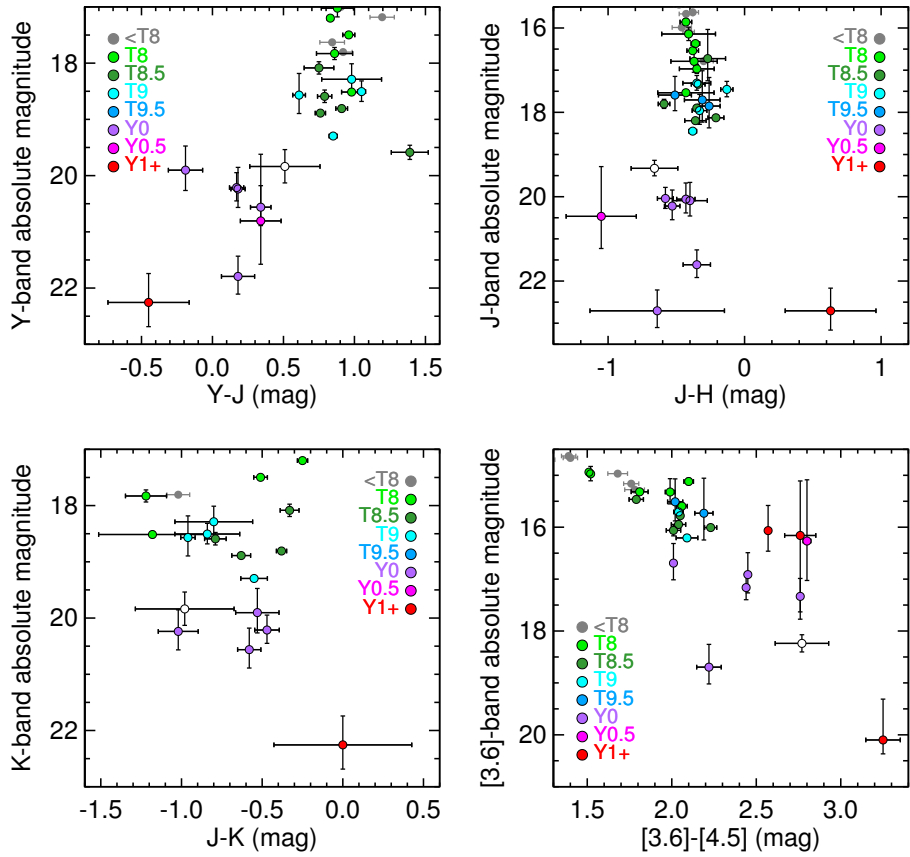


Figure 1: Color–magnitude diagrams for all objects with spectral types T8 and later that have direct distance measurements. Data points are color coded according to spectral type, with open/white points indicating that no spectra are available. Small gray points are earlier type field brown dwarfs. Near-infrared photometry is on the Mauna Kea Observatory (MKO) system.

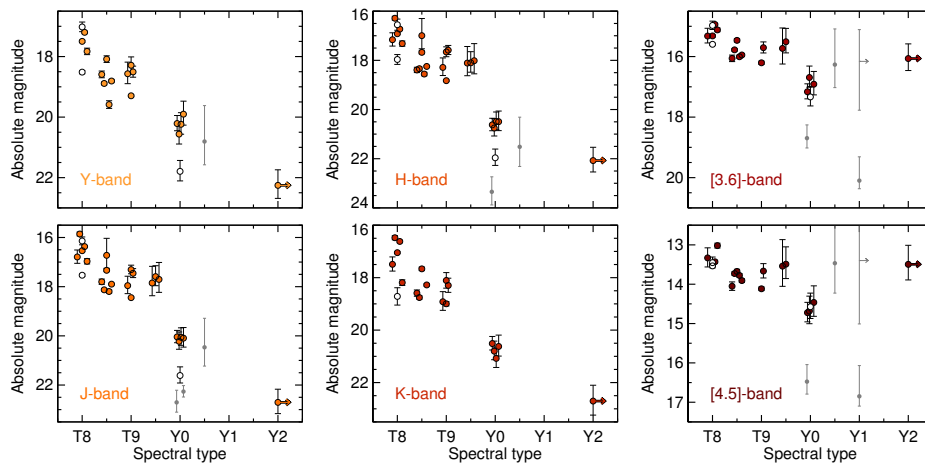


Figure 2: Absolute magnitude as a function of spectral type for near-infrared and mid-infrared bandpasses. Objects typed as peculiar are shown as open white symbols. Objects with very uncertain distances are plotted with smaller gray symbols. Error bars for spectral types are not plotted, and small  $x$ -axis offsets have been added to the spectral types for clarity.

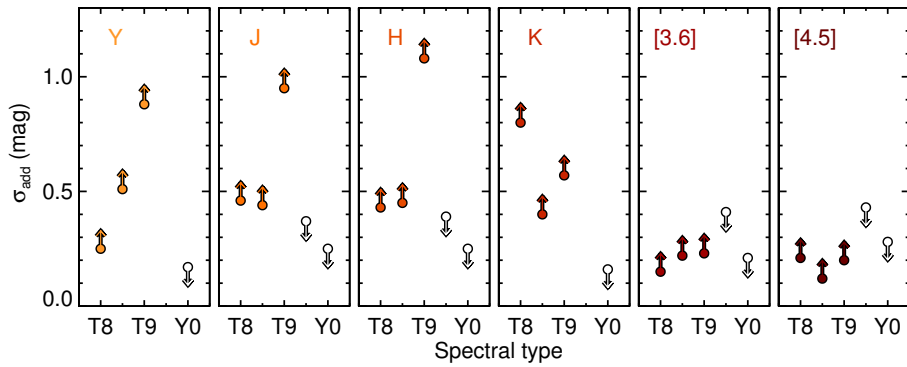


Figure 3: Intrinsic photometric scatter among objects at each spectral type; unfilled symbols are upper limits where no scatter is detected. Y0 dwarfs show remarkably low intrinsic scatter in the near-infrared, reversing the trend observed at the end of the T dwarf sequence that later type T dwarfs show increasing dispersion in their near-infrared absolute magnitudes. The much smaller sample of T9.5 dwarfs are also suggestive of this reversal at *J* and *H* bands. There is no evidence for such a reversal in the mid-infrared where both late-T and Y dwarfs show much less intrinsic scatter and distance uncertainties for Y dwarfs do not permit strong enough upper limits.

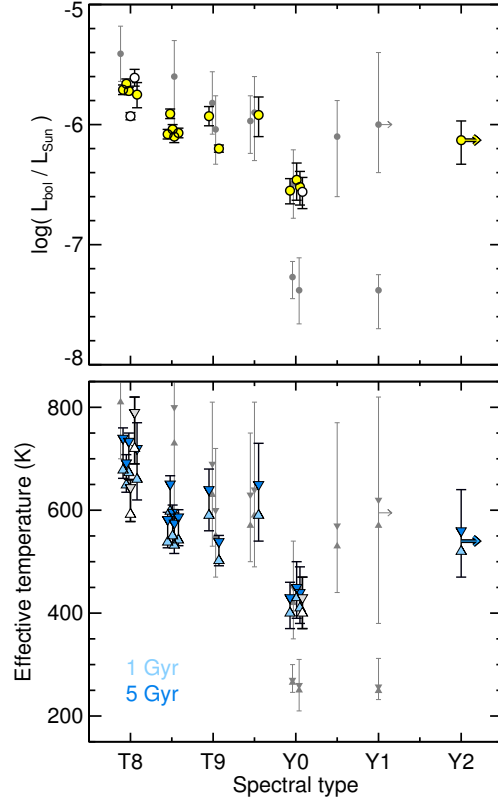


Figure 4: Bolometric luminosities ( $L_{\text{bol}}$ ) and effective temperatures for objects of spectral type T8 and later; spectrally peculiar objects are denoted by white symbols. Objects with  $L_{\text{bol}}$  uncertainties larger than 0.2 dex are shown as smaller, gray symbols. These are either objects with very uncertain distances or the components of tight binaries where the lack of resolved mid-infrared photometry results in a very uncertain bolometric flux. Error bars for spectral types are not plotted, and small  $x$ -axis offsets have been added to the spectral types for clarity. Effective temperatures are derived from our  $L_{\text{bol}}$  measurements and Cond evolutionary model radii. Upward and downward pointing triangles correspond to the median  $L_{\text{bol}}$  and lower and upper age limits used (see Table S5). Error bars show the range of temperatures corresponding to the  $\pm 1\sigma$  range of  $L_{\text{bol}}$  over the same age range.





## Supplementary Materials for

Distances, Luminosities, and Temperatures of the Coldest Known Substellar  
Objects

Trent J. Dupuy<sup>1,2</sup> and Adam L. Kraus<sup>1,3</sup>

<sup>1</sup>Harvard-Smithsonian Center for Astrophysics, 60 Garden St, Cambridge, MA 02138,  
USA

<sup>2</sup>Hubble Fellow

<sup>3</sup>Astronomy Department, University of Texas at Austin, 1 University Station C1400,  
Austin, TX 78712, USA

correspondence to: [tdupuy@cfa.harvard.edu](mailto:tdupuy@cfa.harvard.edu)

**This PDF file includes:**

Materials and Methods  
Supplementary Text  
Figures S1 to S5  
Tables S1 to S6

## Materials and Methods

### Astrometric Monitoring with *Spitzer*

We used the Infrared Array Camera (IRAC) aboard the *Spitzer Space Telescope* (26) in our astrometric monitoring program targeting 16 late-T and Y dwarfs. The data we present here were obtained between 2011 November and 2012 December as part of a Cycle 8 Director’s Discretionary Time program (PID-80233). Our target sample comprises eleven objects that did not have previously published parallaxes, including all six Y dwarfs known in 2011 (3), and five late-T dwarfs with parallax measurements in the literature that serve as a check on our methods.

In the post-cryo (“warm”) *Spitzer* mission, only IRAC channels 1 and 2 at  $3.6\ \mu\text{m}$  and  $4.5\ \mu\text{m}$ , respectively, are operational. Each channel has its own  $256 \times 256$  InSb detector with a pixel scale of  $1''.2\ \text{pixel}^{-1}$ , yielding fields of view of  $5'.2 \times 5'.2$ . We chose to use channel 1, because of the much larger number of reference stars available at shorter wavelengths. The coldest Y dwarfs have extremely red  $[3.6] - [4.5]$  colors due to increased  $\text{CH}_4$  opacity at  $3.6\ \mu\text{m}$  and lowered CO opacity at  $4.5\ \mu\text{m}$ . However, even our faintest target at  $3.6\ \mu\text{m}$  is still bright enough to be detected at high signal-to-noise ratio ( $S/N \gtrsim 20$ ) in a single 100-second IRAC exposure.

We designed our *Spitzer* monitoring program such that each target would be observed at five epochs spanning  $\gtrsim 1.5$  years, as this time baseline allows us to robustly disentangle parallax from proper motion. All targets had previously been observed at least once with *Spitzer*/IRAC  $\gtrsim 1$  year before our program started, enabling us to achieve the needed time baseline and number of epochs with four new observations during Cycle 8. For most of our targets (13 of 16), only two *Spitzer* visibility windows per year are available, each lasting  $\approx 40$ –70 days. For several of these targets, three visibility windows occurred during our program enabling us to obtain one epoch each at the first and last window and two epochs during the middle window. For the remainder we simply obtained two epochs per visibility window. Three targets have one single

$\approx 220$ -day window each year, and for these we obtained epochs spaced uniformly in time. For one target, the T8 dwarf PSO J043.5395+02.3995, we lost a 2012 March epoch due to the extremely large number of radiation hits caused by a solar storm, but the other epoch during that visibility window was unaffected.

### Spitzer Astrometry Pipeline

At each epoch we obtained 9, 18, or 36 dithered images, with more images for fainter targets in order to increase the final S/N of their mean positional measurements. For all of the following analysis we use the “corrected basic calibrated data” products from the automated *Spitzer* pipeline processing. These low-level products have standard corrections applied for detector bias, nonlinearity, pixel-to-pixel response (i.e., flat fielding), and well-understood image artifacts such as column pulldown and muxstripes.

We obtained positional measurements from all sources in each field from the implementation of DAOPHOT (27) in IRAF. The point-spread function (PSF) model used by DAOPHOT was defined within a radius of  $8''$ , and we used a fitting radius of  $5''$ , i.e.,  $3.0 \times$  the  $1''.7$  full-width at half-maximum (FWHM) of IRAC channel 1 images. For `daofind`, we allowed very liberal sharpness and roundness thresholds since the undersampled IRAC images do not constrain these parameters well ( $0 < \text{sharp} < 99$ ;  $-9 < \text{round} < 9$ ), and spurious detections were rejected by clipping later in our analysis. We then used `phot` to measure positions and fluxes for each of the sources from `daofind`, using an aperture of  $2''.5$  and a sky annulus of  $3''.3$ – $5''.8$ . Positions were generated by the default centroiding algorithm using a centering box of  $5''$ . We applied our IRAC distortion solution to the resulting  $(x, y)$  positions directly within IRAF using the routine `xygeotran`, since this is the native environment in which we measured and stored the polynomial coefficients.

We analyzed the resulting position measurements in nearly an identical fashion as in our previous work using ground-based infrared imaging from the Canada-France-Hawaii Telescope

(12). First, we created an astrometric catalog at each epoch by cross-identifying detections and registering the individual dithers. At this initial stage we excluded the lowest S/N detections, applying a threshold in S/N that ranged from 5–10 depending on the data set. (For denser fields we could afford stricter cuts.) Our method for cross-identifying sources used a temporary astrometric solution for the field, created using the *WISE* All-Sky Source Catalog (28). We only kept sources that are detected in  $\geq 50\%$  of our frames, and we  $\sigma$ -clipped these measurements, both of which effectively eliminate spurious detections from appearing in the final astrometric catalog for a given epoch. For positional uncertainties, we used the standard error of the measurements. Next, we registered the astrometry between epochs, masking all sources with large proper motion ( $> 100 \text{ mas year}^{-1}$ ), including the target, during this process. Finally, we determined the absolute astrometric calibration (e.g., pixel scale and orientation) by matching sources with low proper motion to the *WISE* All-Sky Source Catalog.

The properties of each astrometric catalog are given in Table S1, which lists the number of epochs, time baseline, and total number of reference stars as well as the number of reference stars matched with the *WISE* catalog. For our observations, the median astrometric precision per epoch for our targets was 30 mas, with 97% between 20 mas and 40 mas. Our median target S/N was 27, while the first epoch archival data was sometimes of lower S/N and thus had somewhat larger astrometric errors (median of 50 mas and 90% were  $< 60$  mas).

#### Parallaxes and Proper Motions

We determined the proper motions and parallaxes of our targets using essentially the same method as described in Section 2.4 of (12). We found the best-fit solution using MPFIT in IDL (29) and then performed a Markov Chain Monte Carlo (MCMC) analysis using 30 chains each with  $10^6$  steps. The key difference is that we used the JPL ephemeris for *Spitzer* rather than the JPL DE405 ephemeris of the Earth when computing parallax ellipses. In Table S1 we give the parameters derived from our MCMC analysis: right ascension ( $\alpha$ ), declination ( $\delta$ ), parallax

( $\pi_{\text{rel}}$ ), and proper motion ( $\mu_{\alpha} \cos \delta$  and  $\mu_{\delta}$ ). The resulting parameter distributions all appear to be consistent with Gaussians based on fits to their histograms, so we simply quote the median and standard deviation derived from each set of chains. Note that the parallax and proper motion are relative in the sense that the astrometric reference frame for each target is defined by stars at a finite distance and thus has some mean parallax and proper motion. However, even in our shallowest 12-second exposures, the Besançon model of the Galaxy (30) predicts that the mean parallax of our reference stars is 1.5 mas and that 90% of the stars have parallaxes  $< 3$  mas. This is  $\approx 7\text{--}20\times$  smaller than our parallax errors and thus negligible. The  $\chi^2$  of our best-fit solutions are all commensurate with the degrees of freedom ( $\text{dof} = 2 \times N_{\text{epoch}} - 5$ ). This validates our assumed positional uncertainties and derived parameter errors. The best-fit parallax solutions are shown in Fig. S1.

The median parallax precision for our entire sample is 17 mas, and the median fractional uncertainty is 16% or  $S/N = 6.2$ . For 11 of the 16 targets the parallax uncertainty is  $\leq 20\%$  or  $S/N \geq 5.0$ . These parallax errors are currently limited by the available time baseline, not the per epoch astrometric precision, i.e., if the same number and quality of measurements were spread out over more time then the errors would decrease. One control target 2MASS J0415–0935 (T8) has a very long time baseline (8.27 years), as its earliest observations date from the first few months of the *Spitzer* mission. It has similar per epoch precision as other targets but the smallest parallax uncertainty (10 mas), illustrating the point that a long time baseline enables a better determination of the proper motion and thus parallax.

Finally, we note that we visually inspected images from the first and last epochs to determine if our targets may have been blended with background stars during any of our observations. The control T8p dwarf 2MASS J0729–3954 appears in the first epoch to have been passing very close to a star that is  $\approx 1.3$  mag fainter at [3.6]. Given this background star’s position of  $(\alpha, \delta) = (112^{\circ}2488, -39^{\circ}8959)$ , 2MASS J0729–3954 would have passed as close as  $2''.7$  to this

star both in our data and in the Blanco/ISPI imaging used by previous authors to measure its parallax (31). Thus, both of our parallax measurements may be biased by contaminating light from this background star.

### Comparison to Published Parallaxes & Lutz-Kelker Bias

Our five control targets have parallaxes that are in good agreement with published values, providing validation of our methods. The  $\chi^2$  of differences between our parallax values and those previously published is 5.7 (5 dof,  $p = 0.34$ ). The largest discrepancy is for 2MASS J0729–3954 for which previous work found  $\pi = 126 \pm 8$  mas (31) and we find  $91 \pm 25$  mas, which is only a 1.4- $\sigma$  difference and may be due to the contaminating light from a nearby star as noted above. Our other results typically agree within  $1\sigma$  of published values (12, 32–34). Our proper motions typically also agree well, even though these are relative measurements made in a different reference frame than published values. Most proper motions agree within  $1\sigma$ , and the most discrepant value  $\mu_\alpha \cos \delta$  for 2MASSI J0415–0935 ( $3.0\sigma$ ;  $10 \text{ mas year}^{-1}$ ). Seven of our science targets have recently published parallaxes from (35), and the  $\chi^2$  of differences between their values and ours is 5.7 (7 dof,  $p = 0.58$ ). Thus, our parallaxes are in good agreement with the results of (35), but our uncertainties are  $\approx 2\text{--}4\times$  smaller. Our smaller errors are likely due to the fact that we are using a higher quality distortion solution for *Spitzer*/IRAC and  $\sim 10\times$  more reference stars. We also note that most of our proper motion values agree within  $1\sigma$  compared to (35), with three being different by 1.1–2.0 $\sigma$ . A comparison of all our parallaxes to published results is shown in Fig. S2.

One of our science targets, WISEP J1828+2650, has a few different reported parallaxes in the literature. One value of  $122 \pm 13$  mas (8) was based on preliminary results later published in (36), and this is 2.7- $\sigma$  discrepant with our value of  $70 \pm 14$  mas. These authors more recently reported three values based on two different methods of computing relative astrometry (see their Table 7). Their “method 1” gives  $103 \pm 16$  mas, 1.6- $\sigma$  larger than our value, and their “method

2” gives  $79 \pm 12$  mas in good agreement with our parallax (36). A parallax of  $90 \pm 9.5$  mas is also reported based on combining the two methods (36), but we choose not to adopt this value as it likely underestimates the measurement uncertainty. The two methods use the same underlying imaging data and thus are not truly independent data sets, so they cannot simply be combined to reduce the measurement errors. In the following, we use our parallax value for WISEP J1828+2650 since it has a similar uncertainty to the (36) values but is based on data from a single bandpass and telescope, which reduces the chances for systematic errors. In particular, if WISEP J1828+2650 is an unresolved binary with components having different colors, as suggested by (9), then its photocenter would shift between different bandpasses.

Finally, we consider the handful of our targets with low significance parallax detections. One science target WISEP J1541–2250 ( $S/N = 2.4$ ; Y0.5) and one control object Ross 458C ( $S/N = 2.4$ ; T8) have parallax  $S/N < 3$ . As we discuss above, our results for the control objects are in good agreement with the more precise published values. For WISEP J1541–2250, our MCMC analysis gives an upper limit of 148 mas for the parallax at 99% confidence. While our results for this object agree with the new value of  $-21 \pm 94$  mas (35), it is highly discrepant with the earlier measurement from the same group of  $351 \pm 108$  mas (7).

Two additional science targets, WISEP J0148–7202 ( $S/N = 3.8$ ; T9.5) and WISEP J0458+6434 ( $S/N = 3.7$ ; T8.5+T9.5), and one control target 2MASS J0729–3954 ( $S/N = 3.6$ ; T8p) have  $3 < S/N < 5$  parallaxes. For cases of such low  $S/N$ , an assumption that objects are distributed uniformly in space volume would naturally lead to a strong prior in parallax and thereby result in a systematic offset in measured values, i.e., “Lutz-Kelker bias” (37). If other prior information is available, e.g., about absolute magnitudes or velocities, this can be used to mitigate Lutz-Kelker bias, particularly in the lowest  $S/N$  cases where the very steep prior causes zero parallax solutions to dominate for  $S/N \lesssim 4$ , the “Lutz-Kelker catastrophe” (38). However, we do not yet know the expected brightness of Y dwarfs or if their velocity distribution is different

from better studied L and T dwarfs.

Instead, we have investigated the validity of the uniform volume prior given that our science targets were discovered in an all-sky magnitude-limited survey. We simulated this assuming that the underlying absolute magnitudes followed a normal distribution and that objects were distributed uniformly in space. The resulting distance distributions when applying a selection cut in apparent magnitude are shown in Fig. S3. These are all essentially lognormal distributions of differing widths that have a tail at small distances that matches a uniform volume prior. Thus, the slope of the prior, i.e., whether large or small distances are preferred, actually depends on where the object is with respect to the magnitude limit of the survey, and this would require a prior assumption for its absolute magnitude. If most objects are found near the survey limits, as is usually the case, a roughly flat prior corresponding to the peaks of these distributions would actually be most appropriate. Since we do not know the absolute magnitudes Y dwarfs a priori, we conservatively choose to adopt a simple, uniform prior in the parallax. This approach is supported by a test using the two control objects with low significance parallaxes. For 2MASS J0729–3954 and Ross 458C we tried a uniform volume prior in our MCMC analysis by adding  $4 \log(\pi/\pi_{\text{best-fit}})$  to the  $\chi^2$  and found that the resulting parallaxes were brought out of agreement with literature values under such a prior.

### Absolute Magnitudes

In Table S2, we have compiled the available near- and mid-infrared photometry for our sample as well as all other objects of spectral types T8 or later with distance measurements. For the mid-infrared we use *Spitzer*/IRAC photometry since it is typically of much higher S/N than *WISE* catalog photometry for the latest type sources, which are often not detected in the *W1* band that is similar to IRAC’s [3.6] band. We have supplemented *Spitzer* photometry from the literature by performing aperture photometry on archive images of PSO J043.5+02.39 (T8). The only other objects without *Spitzer* photometry are WISE J1639–6847 (Y0:) and



the components of the tight binaries 2MASSW J1225–2739 (T5.5+T8), WISEP J0458+6434 (T8.5+T9.5), WISEP J1217+1626 (T9+Y0), and CFBDSIR J1458+1013 (T9+Y?) that are unresolved in *Spitzer* images. For near-infrared photometry we use the results of (9) where possible for the Y dwarfs, otherwise photometry from (7, 8). These published results are all on the Mauna Kea Observatories (MKO) photometric system, except for WISEP J1741+2553, which is on the 2MASS system. We computed MKO–2MASS offsets of  $J_{\text{MKO}} - J_{2\text{MASS}} = -0.30$  mag,  $H_{\text{MKO}} - H_{2\text{MASS}} = 0.07$  mag, and  $K_{\text{MKO}} - K_{s,2\text{MASS}} = 0.13$  mag for this object from its Magellan/FIRE spectrum published by (7). The resulting color–magnitude diagrams are shown in Fig. 1 where we include earlier type field dwarfs from our Database of Ultracool Parallaxes for context.<sup>1</sup>

In Table S3, we give mean absolute magnitudes for each spectral type bin, along with a lower or upper limit on the amount of intrinsic scatter in each bin, depending on whether the rms in the magnitudes is consistent with that expected from measurement uncertainties or not, i.e.,  $p(\chi^2) \geq 0.5$  or  $p(\chi^2) < 0.5$ , respectively. Note that we chose a  $p$ -value cutoffs of 0.5/0.5 here rather than 0.95/0.05 or 0.05/0.95 since we do not know a priori whether to expect significant intrinsic scatter or not. The null hypothesis is not necessarily that there should be zero intrinsic scatter, since earlier spectral types often (but not always) show significant scatter in absolute magnitudes (12). These upper/lower limits on the intrinsic photometric scatter at each spectral type are shown in Fig. 3. We excluded from our table of mean magnitudes and the discussion here two Y0 dwarfs that have unreliable parallaxes, WISE J0359–5401 and WISE J1639–6847.

In our analysis we use the tabulated mean absolute magnitudes rather than polynomial fits as a function of spectral type that are commonly used in other work (8, 35). This is because smooth polynomials often do not accurately capture changes in absolute flux with spectral type. At spectral types of T8, T8.5, and T9, our mean absolute magnitudes are within  $\pm 0.3$  mag of

---

<sup>1</sup>Maintained by T. Dupuy at <http://www.cfa.harvard.edu/~tdupuy/plx>; updated 2012-06-09.

the polynomial relation between  $H$ -band absolute magnitude and spectral type that excludes WISEP J1828+2650 ( $\geq Y2$ ) from (8). Since we find that T9.5 dwarfs are brighter than Y0 dwarfs, which is impossible to capture with the smooth polynomial from (8), our mean value is 1.8 mag brighter than their relation at this spectral type. Finally, our mean  $H$ -band fluxes for Y0 dwarfs are 0.6 mag brighter than the polynomial from (8). This is simply due to the polynomial undershooting their data points that happen to be very similar to ours, despite updated distances since their preliminary parallaxes and improved photometry from (9).

### Calculating Bolometric Luminosities

As little as  $\lesssim 3\%$  of the emergent flux of Y dwarfs is expected to be emitted in the standard near-infrared windows at  $YJHK$ , and no existing facilities are capable of measuring the spectra of Y dwarfs in the mid-infrared where they emit most of their light. Therefore we must rely on models to some extent when deriving bolometric luminosities for our sample, since we cannot directly integrate the observed SEDs. Fortunately, the available photometry typically captures  $\gtrsim 50\%$  of the bolometric flux, which helps weaken this dependence on models.

Rather than use a single bandpass, we develop a method of summing the fluxes from individual bandpasses to compute “super-magnitudes” that combine both mid-infrared and near-infrared flux when possible. To have as much uniformity in our  $L_{\text{bol}}$  calculations as possible, we chose filter combinations for which the largest subsets of targets have available photometry. All single objects earlier than Y1 in our sample have photometry in  $J$ ,  $H$ , [3.6], and [4.5] bands, so this defined the main super-magnitude we used ( $m_{JH12}$ ).<sup>2</sup> Note that adding  $K$ -band data would not contribute much additional flux, since it typically contains  $\lesssim 10\%$  the total  $J+H$  flux for such cool objects. At the very latest types ( $\geq Y1$ ), near-infrared photometry is usually not available so we used only a sum of the [3.6]- and [4.5]-band flux ( $m_{12}$ ).

---

<sup>2</sup>The Vega zero points we used to convert magnitudes into fluxes for  $\{Y, J, H, K, [3.6], [4.5]\}$  bands were, respectively,  $\{5.690, 4.322, 3.139, 1.318, 0.456, 0.235\} \times 10^{-7} \text{ erg cm}^{-2} \text{ s}^{-1}$ . The zero-points for our super-magnitudes are simply the sum of the Vega fluxes, e.g., for  $m_{JH12}$  this would be  $8.152 \times 10^{-7} \text{ erg cm}^{-2} \text{ s}^{-1}$ .

We used model atmospheres (*11*, *15*) to compute bolometric corrections for the super-magnitudes  $m_{JH12}$  and  $m_{12}$ . To span the possible range of properties for our sample, we used models with temperatures of  $\{300, 400, 500, 600, 700\}$  K and surface gravities of  $\{1, 3, 10\} \times 10^4 \text{ cm s}^{-2}$ . We used models with cloud sedimentation parameters ranging from  $f_{\text{sed}} = 2-5$ , i.e., thick to thin clouds (*11*), as well as corresponding cloud-free models (*15*). Fig. 9 of (*11*) shows that at gravities of  $10^4$  and  $3 \times 10^4 \text{ cm s}^{-2}$  the  $f_{\text{sed}} = 3, 4, 5$ , and cloud-free models agree best with the properties of late-T dwarfs on near-infrared color magnitudes, and for  $g = 10^5 \text{ cm s}^{-2}$  the  $f_{\text{sed}} = 4, 5$ , and cloud-free models agree best. Therefore, we used only these subsets of cloud parameters, and this resulted in 47 different models being used to calculate bolometric corrections. We took the mean and standard deviation of the derived values and found  $BC_{JH12} = 2.93 \pm 0.08 \text{ mag}$  and  $BC_{12} = 5.29 \pm 0.21 \text{ mag}$  (Fig. S4). (Note that we initially tried larger ranges of model parameters but found that they did not significantly change the resulting bolometric corrections, since most of the flux is already captured by the super-magnitudes.) For future reference, we also computed bolometric corrections using bands 1 and 2 of *WISE* instead of IRAC. We calculate a  $J+H+W1+W2$  bolometric correction of  $2.93 \pm 0.06 \text{ mag}$  and  $W1+W2$  bolometric correction of  $5.12 \pm 0.21 \text{ mag}$ , assuming model magnitude zero points of  $5.751 \times 10^{-8} \text{ erg cm}^{-2} \text{ s}^{-1}$  for *W1* and  $2.527 \times 10^{-8} \text{ erg cm}^{-2} \text{ s}^{-1}$  for *W2*.

In order to derive bolometric luminosities for objects without mid-infrared photometry, mostly components of tight binaries, we derived bolometric corrections for near-infrared magnitudes alone. Rather than rely directly on models, we used the apparent bolometric magnitudes ( $m_{\text{bol}}$ ) of the single objects that have mid-infrared photometry to compute bolometric corrections at *Y*, *J*, *H*, and super-magnitudes of *Y+J*, *J+H*, and *Y+J+H*. We then took the weighted average at each spectral type, and these values are reported in Table S4. The rms about these mean values was 0.6 mag for all filter combinations, and we consider this to be the uncertainty in these bolometric corrections. As expected, the scatter is much higher with-

out mid-infrared photometry, since even  $Y+J+H$  captures only  $\approx 10\%$  of the bolometric flux. However, this method arrives at much more precise bolometric corrections than are possible using models alone (e.g., if we used models as above but for a  $YJH$  super-magnitude we would derive  $BC_{YJH} = 0.9 \pm 1.2$  mag).

In Table S5 we list the apparent bolometric magnitudes derived for our sample along with the final bolometric luminosities, where  $\log(L_{\text{bol}}/L_{\odot}) \equiv (4.7554 - m_{\text{bol}} + 5 \log d - 5)/2.5$ , where  $d$  is the distance in parsecs.<sup>3</sup> We quote  $m_{\text{bol}}$  and  $L_{\text{bol}}$  separately so that improved parallax measurements in the future can be readily applied to compute new luminosities. In Fig. 4 we plot our derived  $L_{\text{bol}}$  values as a function of spectral type. As a test of our methods, we check the two T8 dwarfs with published values for  $L_{\text{bol}}$  based on near-infrared and mid-infrared spectra. The published values of  $\log(L_{\text{bol}}/L_{\odot}) = -5.67 \pm 0.02$  dex for 2MASSI J0415–0935 (39) and  $-5.69 \pm 0.03$  dex for 2MASS J0939–2448 (40) are more precise than our values and agree well with our derived luminosities, within  $1.3\sigma$  and  $0.4\sigma$ , respectively. In the following analysis, we use our  $L_{\text{bol}}$  values for these two objects for consistency when comparing results among the rest of the sample.

### Deriving Effective Temperatures and Other Fundamental Properties

Effective temperature is defined as  $T_{\text{eff}} \equiv (4\pi\sigma R_{\star}^2/L_{\text{bol}})^{-1/4}$ , where  $\sigma$  is the Stefan–Boltzmann constant. We can therefore derive effective temperatures for our sample late-T and Y dwarfs using our measured luminosities and an assumption for their radii. Evolutionary models (16, 41) generally agree well with the measured radii of transiting substellar objects over a wide range of masses from  $\approx 5$ – $60 M_{\text{Jup}}$  (4–6, 42). We note that transiting objects in the  $\approx 5$ – $20 M_{\text{Jup}}$  mass range that we are most interested in may have formed via core accretion or have been subjected to intense stellar irradiation over their lifetimes, either of which could alter their

---

<sup>3</sup>The bolometric absolute magnitude of the Sun is from <http://www.pas.rochester.edu/~emamajek/sun.txt>. Note that we also recompute the model  $\log(L_{\text{bol}}/L_{\odot})$  values from radius and  $T_{\text{eff}}$  using the corresponding solar luminosity of  $3.827 \times 10^{33}$  erg s<sup>−1</sup> for consistency.

radii compared to the solar-abundance, gas-only evolutionary models relevant for our sample. However, despite the fact that they may not be ideal test cases, the ensemble of measurements to date display the expected trends that more intensely irradiated objects are inflated compared to non-irradiated models (43) and massive objects most likely to be entirely gaseous and least likely to be affected by irradiation agree well with models (44). Furthermore, we note that observed variations in radii compared to models are relatively small and similar to the variations predicted over the range of plausible ages and masses. Evolutionary models fortuitously predict that the mass–radius relationship is nearly flat with maximal variations of only  $\pm 15\%$  over more than an order of magnitude in mass ( $5\text{--}80 M_{\text{Jup}}$ ). At ages typical for field brown dwarfs, radii are predicted to contract by only  $\approx 5\%$  at a given mass from 1 Gyr to 5 Gyr, although we note that for much younger ages their radii can be substantially larger (e.g.,  $10\%\text{--}20\%$  larger at 0.1 Gyr relative to 1 Gyr for masses of  $5\text{--}20 M_{\text{Jup}}$ ). Ultimately, any variations in radius have a comparatively small impact on our derived temperatures since  $T_{\text{eff}} \propto R_{\star}^{-1/2}$ .

We use the Cond evolutionary model isochrones (16) at ages of 1 Gyr and 5 Gyr to derive radii, temperatures, masses, surface gravities, and deuterium abundances for our sample. We interpolate the logarithm of these quantities from each isochrone as a function of  $\log(L_{\text{bol}})$ . We have chosen these models because they are among the most widely used models that are appropriate for objects that have no silicate condensate clouds in the photosphere. In principle, clouds at earlier stages of evolution can have some impact on properties at older ages, but the available models accounting for such effects do not currently extend to low enough luminosities (45). New evolutionary models are currently being developed that not only account for silicate cloud evolution but previously neglected sulfide clouds (11). As an example of the differences between evolutionary models with varying boundary conditions and interior structure physics, the predicted radii from (45) are  $3\%\text{--}5\%$  higher over the  $5\text{--}30 M_{\text{Jup}}$  mass range at 1 Gyr compared to Cond models. This contributes a negligible uncertainty of  $1.5\%\text{--}2.5\%$  to

our derived temperatures.

In Table S5 we list the model-derived properties for each object, with uncertainties given solely by the individual luminosity errors propagated through the interpolation of the models. Note that these error bars therefore only reflect the rms in the parallaxes and bolometric corrections at a given age and do not include any potential systematic errors in our bolometric corrections or in the evolutionary model isochrones. In Table S6, we report weighted averages as a function of spectral type for the luminosities and model-derived properties of “normal” objects. We do not report individual values of the deuterium abundance relative to the initial abundance ( $D/D_0$ ), since it is typically either zero or unity. The Cond models predict that at 1 Gyr objects should have retained nearly all of their initial deuterium for  $T_{\text{eff}} \leq 500$  K and should have depleted almost all of it for  $T_{\text{eff}} \geq 615$  K. At 5 Gyr, Cond models predict that deuterium boundary lies at  $T_{\text{eff}} = 320\text{--}390$  K, i.e., cooler than we find for normal T8–Y0 dwarfs at that age. We note that this is a potential test of the ages/masses of this sample, since an older, i.e., higher mass, population of Y0 dwarfs should show no evidence of deuterium, whereas younger objects of similar temperature would retain most or all of their deuterium.

A few objects in our sample are companions to more massive stars with independent age constraints. Ross 458AB has an age in the range 150–800 Myr based on strong chromospheric activity and a lack of spectroscopic signatures of very low surface gravity (24). Thus, we used these ages instead of 1 Gyr and 5 Gyr to derive properties from the Cond models. (Note that on the extreme ends of this age range, Ross 458C is expected to retain all or none of its initial deuterium.) WD 0806–661A has a white dwarf cooling age of  $2.0 \pm 0.5$  Gyr (25), and thus we use ages of 1.5 Gyr and 2.5 Gyr for WD 0806–661B. The other companions, Wolf 940B at 3.5–6.0 Gyr (46), BD+01 2920B at 2.3–14.4 Gyr (47), and WISE J1118+3125 at 2–8 Gyr (48), have ages that are not well constrained but are broadly consistent with one or both of our fiducial ages of 1 Gyr and 5 Gyr, so we do not calculate separate properties for these objects.

In Fig. 4 we show our derived effective temperatures as a function of spectral type. The mean luminosity for T8 dwarfs is in good agreement with previous estimates based on more extensive SED coverage,  $\log(L_{\text{bol}}/L_{\odot}) = -5.70$  dex, and at ages of 1 Gyr and 5 Gyr this corresponds to 685 K and 745 K, respectively. Normal Y0 dwarfs have a mean temperature of 410 K and 440 K for assumed ages of 1 Gyr and 5 Gyr. They are more than an order of magnitude less luminous than T8 dwarfs, and correspondingly  $T_{\text{eff}}$  drops by 40% and masses are predicted to be lower by a factor of  $\approx 2$ . (Note that evolutionary models predict that radii increase by  $\approx 20\%$  with decreasing mass over the range  $\approx 5\text{--}60 M_{\text{Jup}}$ , so this slightly counteracts the trend of lower luminosity objects at a given age having lower  $T_{\text{eff}}$ .)

The temperatures of Y0 dwarfs, despite being much cooler than their late-T counterparts, are significantly warmer than found by model atmosphere fitting (3). In Fig. S5 we show these published temperatures for objects in common with our parallax sample. For four “normal” Y0 dwarfs (including WISEP J1541–2250, which is now classified as Y0.5), model atmosphere best fits give 350 K (3). The  $T_{\text{eff}}$  range of plausible model fits were 350–400 K in two cases (350 K only in the others) with best-fit gravities ranging from  $\log g = 3.75$  to 4.75 (cgs) (3).

## Supplementary Text

### Tangential Velocities

Proper motions combined with distance measurements directly yield velocities in the tangent plane of the sky ( $V_{\text{tan}}$ ). For earlier type late-M, L, and T dwarfs, the median and rms is  $V_{\text{tan}} \approx 30 \pm 20 \text{ km s}^{-1}$  (49) computed from samples of  $\sim 100$  objects per spectral class with measured proper motions and spectroscopic distance estimates. Two Y dwarfs have published values of  $V_{\text{tan}} \gtrsim 100 \text{ km s}^{-1}$  (7), suggesting that this population may have significantly higher  $V_{\text{tan}}$  than T dwarfs.

For our entire sample of T8 or later objects, we find a weighted mean  $V_{\text{tan}} = 23 \text{ km s}^{-1}$  with

an rms of  $27 \text{ km s}^{-1}$ , which is generally consistent with earlier type objects (49). For just the Y0 dwarfs, we find a weighted mean of  $V_{\text{tan}} = 45 \text{ km s}^{-1}$  and rms of  $30 \text{ km s}^{-1}$ , both slightly higher than at earlier types but not as high as initial published estimates (7). This is partly because our parallax distances are 10%–20% closer than earlier photometric distance estimates, but also because the earlier proper motion precision was not sufficient to measure  $V_{\text{tan}}$  for the slower moving objects in the sample. Note that the  $30 \text{ km s}^{-1}$  rms we report for our sample includes scatter due to measurement error, and the mean error in  $V_{\text{tan}}$  for Y0 dwarfs is  $9 \text{ km s}^{-1}$ . In computing the mean and rms we considered only free-floating late-type systems, i.e., excluding companions to stars or other brown dwarfs, like Ross 458C and WISEP J1217+1626B. We also exclude three Y0–Y1 dwarfs that only have parallaxes and proper motions from (35), since those authors used the  $V_{\text{tan}}$  distribution of T dwarfs as a prior in their Bayesian astrometric analysis, thus their  $V_{\text{tan}}$  values are technically not independent of that prior.

We have checked if any objects in our sample could be likely members of the thick disk or halo populations on the basis of having very high  $V_{\text{tan}}$ . Using criteria provided by (12) for determining if objects are likely non-thin disk members, we find that none of our sample fit the criterion for  $p_{\text{thin}} < 0.1$ . The two objects with the most significant high  $V_{\text{tan}}$  measurements are PSO J043.5+02.39 (T8;  $91^{+12}_{-10} \text{ km s}^{-1}$ ) and WISEP J0410+1502 (Y0;  $87^{+12}_{-10} \text{ km s}^{-1}$ ), which are the only objects that do not satisfy the  $p_{\text{thin}} > 0.9$  thin disk criterion from (12). The only object with nominally higher  $V_{\text{tan}}$  than these two objects is WISEP J0148–7202 (T9.5;  $99^{+40}_{-23} \text{ km s}^{-1}$ ), but its distance is currently very uncertain ( $S/N = 3.8$ ).

### Beyond Y0

There are four objects with distance measurements that are classified as having spectral types later than Y0. Two of these are in our *Spitzer* sample, WISEP J1541–2250 (Y0.5) and WISEP J1828+2650 ( $\geq$ Y2), and the other two only have parallaxes from (35), WISE J0350–5658 (Y1) and WISE J0535–7500 ( $\geq$ Y1). These latter two have parallax  $S/N$  of 5.8 and 3.2, re-



spectively, but (35) report distances having  $1.6\text{--}1.8\times$  lower S/N after applying their Bayesian priors. This makes the distance of WISE J0535–7500 particularly uncertain, since its parallax of  $250 \pm 79$  mas implies a distance of 4 pc but its quoted final distance is  $21_{-11}^{+13}$  pc after applying priors (35). Therefore we focus on the two objects with more robust distances in the following.

WISEP J1541–2250 (Y0.5) was originally reported as a Y0 dwarf at 2.8 pc based on a preliminary parallax of  $350 \pm 110$  mas (7). In previous work it has thus often appeared as an extremely faint data point  $\approx 5\text{--}6$  mag below the end of the T dwarf sequence. The same team has since revised its spectral type to Y0.5 (8) and parallax to  $-21 \pm 94$  mas (35). Our parallax of  $74 \pm 31$  mas is the most precise yet but still too low S/N to securely determine its location relative to T8–Y0 dwarfs. It now appears to be only  $\approx 2$  mag fainter than the end of the T sequence in the near-infrared, and its absolute magnitude is consistent with Y0 dwarfs in the near-infrared and with all T8–Y0 dwarfs in the mid-infrared. Its  $YJH$  colors also appear to be consistent with other Y0 dwarfs, while its  $[3.6] - [4.5]$  color is slightly redder than the reddest Y0, the peculiar WISEP J1405+5534.

WISE J0350–5658 is defined as the spectral standard for the Y1 class (8). This object does not have  $YJHK$  photometry, but on mid-infrared color–magnitude diagrams it is the reddest known object, with  $[3.6]$  and  $[4.5]$  absolute magnitudes  $\approx 2\text{--}3$  mag and  $\approx 1\text{--}2$  mag fainter ( $1\sigma$  ranges), respectively, compared to Y0 dwarfs. Thus, it would appear that while  $L_{\text{bol}}$  does not drop substantially going from Y0 to Y0.5, it plummets going from Y0.5 to Y1. Unfortunately, these Y0.5–Y1 objects have some of the lowest significance distance measurements, and the sample is very small, so it is unclear if these trends will turn out to be real. At face value, WISE J0350–5658 (Y1) would be the least luminous and thus coldest (230–300 K) object in the entire sample, aside from two objects with very uncertain parallaxes, WISE J1639–6847 and WISE J0359–5401. Therefore, it is remarkable that the near-infrared spectrum of WISE J0350–5658 (8) is only subtly different from other Y dwarfs that are nomi-

nally  $\approx 150$  K ( $1.6\times$ ) warmer.

WISEP J1828+2650 has the highest precision distance of any object later than Y0 ( $14.3_{-2.4}^{+3.6}$  pc). It was originally typed as  $>Y0$  (3) but has been re-classified as  $\geq Y2$  (8) in the context of a larger sample of near-infrared spectra. WISEP J1828+2650 has singular properties not observed in any other Y dwarf, and thus it has been the subject of extensive discussion in the literature. WISEP J1828+2650 has been dubbed the archetype for the Y spectral class in prior work that ascribes its unusually red  $J - H$  and near-infrared minus mid-infrared colors to the collapse of flux as the Wien tail moves into the near-infrared (3). WISEP J1828+2650 is also the only known object to show a suppressed  $J$ -band, i.e.,  $1.27 \mu\text{m}$ , flux peak. These authors estimated an upper limit of  $T_{\text{eff}} \lesssim 300$  K based on a comparison of the observed properties to predictions from atmospheric models (3). In subsequent work, a preliminary parallax of  $122 \pm 13$  mas for WISEP J1828+2650 to compute its absolute magnitudes (8). This parallax is  $3.4\sigma$  larger than the final value determined by (36) and  $2.7\sigma$  larger than our *Spitzer*-only parallax. Even using the closer distance, (8) found that WISEP J1828+2650 had similar or brighter magnitudes than Y1 dwarfs in the near-infrared and surprisingly was as bright as Y0 dwarfs in the mid-infrared. They suggested that if this rebounding of the flux relative to earlier type objects is not a real effect, then it may be due either to systematic errors in their preliminary parallaxes, misclassification of the type for WISEP J1828+2650, or some unknown physical cause. Our updated parallax places WISEP J1828+2650 even farther away, intensifying this puzzle as its mid-infrared magnitudes are even brighter than the earlier type Y dwarfs. Other authors have pointed out that for such large amount of flux to be produced by an object with  $T_{\text{eff}} \lesssim 300$  K would require an unusually large radius, implying a very young age of  $\lesssim 50$  Myr and low mass of  $\lesssim 1 M_{\text{Jup}}$  (9). They suggested instead that WISEP J1828+2650 is an unresolved binary composed of 300 K and 325 K components with types of Y1 and Y1.5 (9). While this helps explain its mid-infrared flux somewhat, bringing it into better agreement with models, it does not ex-

plain the unusually red  $J - H$  color and unique near-infrared spectral morphology. Recent work fitting the  $H$ - and  $[4.5]$ -band absolute magnitudes of WISEP J1828+2650 to Cond model isochrones has found  $T_{\text{eff}} = 275 \pm 40$  K and  $T_{\text{eff}} = 450 \pm 40$  K, respectively (36). These authors conclude that the nature of WISEP J1828+2650 is currently ambiguous due to the fact that no models consistently reproduce its properties (36). It has also been suggested that low metallicity may be partly responsible for some of the unusual properties of WISEP J1828+2650 (50).

We find that WISEP J1828+2650, with  $\log(L_{\text{bol}}/L_{\odot}) = -6.13_{-0.16}^{+0.20}$  dex, is at least as luminous as normal Y0 dwarfs, which have a mean  $\log(L_{\text{bol}}/L_{\odot})$  of  $-6.52$  dex. Our approach of summing the near-infrared and mid-infrared fluxes to estimate the bolometric luminosity is distinct from prior work, since it greatly reduces the dependence of our results on predicted colors and magnitudes from models. WISEP J1828+2650 cannot be much less luminous than we have estimated since we directly account for  $(1.3_{-0.4}^{+0.8}) \times 10^{27}$  erg s $^{-1}$  of its luminosity from photometry alone, which is equivalent to  $\log(L_{\text{bol}}/L_{\odot}) = -6.45_{-0.16}^{+0.19}$  dex. If WISEP J1828+2650 is indeed cooler than other Y dwarfs, it must have a very large radius. To agree with the 300 K upper limit in  $T_{\text{eff}}$  proposed by (3) would require  $R_{\star} = 3.1_{-0.5}^{+0.8} R_{\text{Jup}}$  (or  $0.32_{-0.05}^{+0.08} R_{\odot}$ ), which is  $3.5\sigma$  larger than Cond model radii even for an age of 10 Myr. We therefore suggest that such an explanation is unphysical and that the temperature of WISEP J1828+2650 is indeed warmer than expected from comparison to model spectra. Our calculations give  $T_{\text{eff}} = 520_{-50}^{+60}$  K and  $560_{-60}^{+80}$  K at ages of 1 Gyr and 5 Gyr, respectively. Even if we split the flux into two hypothetical binary components as proposed in Table 7 of (9), we find  $T_{\text{eff}} = 440_{-40}^{+60}$  K and  $420_{-40}^{+60}$  K at 1 Gyr and  $T_{\text{eff}} = 470_{-50}^{+70}$  K and  $450_{-40}^{+60}$  K at 5 Gyr. Thus, regardless of whether or not it is an unresolved binary, we find that WISEP J1828+2650 is as warm or warmer than Y0 dwarfs. We note that it could still be slightly younger than the Y0 dwarfs, and indeed models show that the collapse of the near-infrared flux due to the Wien tail happens at warmer  $T_{\text{eff}}$  when the surface gravity is lower even up to ages of 5 Gyr (23).

## Notes on Individual Objects

We now discuss the handful of objects that are thought to be spectrally peculiar, are lacking spectral types, or that otherwise stand out as atypical.

- 2MASSW J1225–2739B (T8): This is the brightest T8 dwarf in our sample by  $\approx 0.6$  mag in the near-infrared. If this object is an unresolved binary it would make this system a triple. However, we note that its T8 spectral type was not determined using resolved spectroscopy of the individual components, like most other objects in our sample but rather by a spectral decomposition technique matching summed template spectra to its integrated-light spectrum, constrained by the measured near-infrared flux ratios which has a quoted uncertainty of  $\pm 0.5$  subtypes (12). This is consistent with previous estimates of  $T8 \pm 1$  based on optical colors (51) and  $T7.5 \pm 0.5$  from near-infrared magnitudes (52). Thus, a simpler solution to its apparent overluminousness would be that its spectral type is T7.5, not T8, since this would make its near-infrared magnitudes agree very well with the mean properties of other normal T7.5 dwarfs (12).
- UGPS J0722–0540 (T9): This object is defined as the spectral standard for the T9 class (3). However, its location on color–magnitude diagrams is notably distinct from the other three T9 dwarfs (Fig. 1); its absolute magnitudes are  $\approx 0.8$  mag fainter in the near-infrared and  $\approx 0.6$  mag fainter in the mid-infrared, and its derived  $T_{\text{eff}} \approx 500\text{--}550$  K is correspondingly  $\approx 100$  K lower. As more parallaxes for T9 dwarfs are obtained, it should become clear whether UGPS J0722–0540 is indeed unique or if the T9 subclass simply shows an unusual amount of diversity.
- WISEP J1405+5534 (Y0p): This object has similar mid-infrared absolute magnitudes to normal Y0 dwarfs, but our parallaxes show that it is  $\approx 1.5$  mag fainter in the near-infrared. Thus, we find it has essentially the same luminosity and temperature as other

Y0 dwarfs, but different underlying properties. At discovery this object was typed as peculiar (“pec?”) due to the fact that its spectrum’s  $H$ -band peak is shifted  $60 \text{ \AA}$  redder than the Y0 standard WISEP J1738+2732 (3). If this shift is due to enhanced  $\text{NH}_3$  absorption as compared to other Y0 dwarfs of the same  $T_{\text{eff}}$ , we suggest this may imply a reduced level of nonequilibrium chemistry in the photosphere, perhaps due to reduced vertical mixing. This would be also be consistent with the fact that WISEP J1405+5534 is the reddest Y0 dwarf in  $[3.6] - [4.5]$ , which implies enhanced  $\text{CH}_4$  absorption and reduced CO absorption. However, it is not clear how this would lead to a  $\approx 1.5$  mag flux drop in the  $YJHK$  bands but no difference in the mid-infrared flux.

- WISE J0359–5401 (Y0): This object only has a parallax from (35), who find  $145 \pm 39$  mas and  $d = 5.9_{-0.8}^{+1.3}$  pc after applying their Bayesian priors. However, we find it implausible that the precision in the distance ( $S/N = 5-7$ ) could actually be higher than the parallax ( $S/N = 3.7$ ), and thus we have excluded this object from our analysis until a more precise parallax is available. (At the quoted distance from (35), WISE J0359–5401 would be the faintest known Y dwarf, 2–3 mag fainter in both near-infrared and mid-infrared bands as compared to other Y0 dwarfs.)
- WISE J1639–6847 (Y0): This object has a preliminary parallax of 200 mas based on three epochs spanning three months in 2012 using the near-infrared camera FourStar at Magellan combined with two *WISE* epochs (53). The formal parallax uncertainty is 12 mas, and these authors adopt an error of 20 mas (53). This object only has  $J$ -band photometry, and the preliminary distance implies that it would be  $\approx 2$  mag fainter than normal Y0 dwarfs. Using the same rationale as for WISE J0359–5401 above, we have excluded this object from our analysis until a parallax is measured with longer time baseline data.

- CFBDSIR J1458+1013B: This object was discovered by (2), who speculated that its low luminosity and unusual near-infrared colors might ultimately lead it to be classified as a Y dwarf. A spectrum for this  $0''.11$  binary companion is not available; however, we can now compare its near-infrared absolute magnitudes to those of other Y dwarfs. On various  $YJHK$  color–magnitude diagrams, it appears to be slightly brighter than or consistent with Y0 dwarfs. CFBDSIR J1458+1013B is  $\approx 1$  mag fainter than the faintest T9 dwarf and 0.4–0.7 mag brighter than the mean of normal Y0 dwarfs. Thus, we find that it is more likely to be an early Y dwarf than a very late T dwarf, and we suggest using a photometric spectral type estimate of Y0.
- WD 0806–661B: This object has only been detected in two bandpasses, [3.6] and [4.5]. According to our estimate of  $\log(L_{\text{bol}}/L_{\odot}) = -6.81 \pm 0.09$  dex, this would be the least luminous object known to date, possibly except for a few objects that have very uncertain distances (WISE J0350–5658, WISE J0359–5401, and WISE J1639–6847). Using the white dwarf cooling age from WD 0806–661A and Cond models we find  $T_{\text{eff}} = 353^{+23}_{-22}$  K, slightly higher than the 300–345 K suggested by (25) based on their comparison of the [4.5]-band absolute magnitude and  $J$ -band nondetection to models of (23, 45). As these authors point out, the models do not reproduce the location of WD 0806–661B on mid-infrared color–magnitude diagrams (25), so using a single-band flux measurement for their  $T_{\text{eff}}$  is likely less robust than using the combined flux in both *Spitzer* bandpasses as we have done. As discussed above, the case of WISEP J1828+2650 also highlights the perils of inferring fundamental properties from model predicted colors and magnitudes for such cool objects.

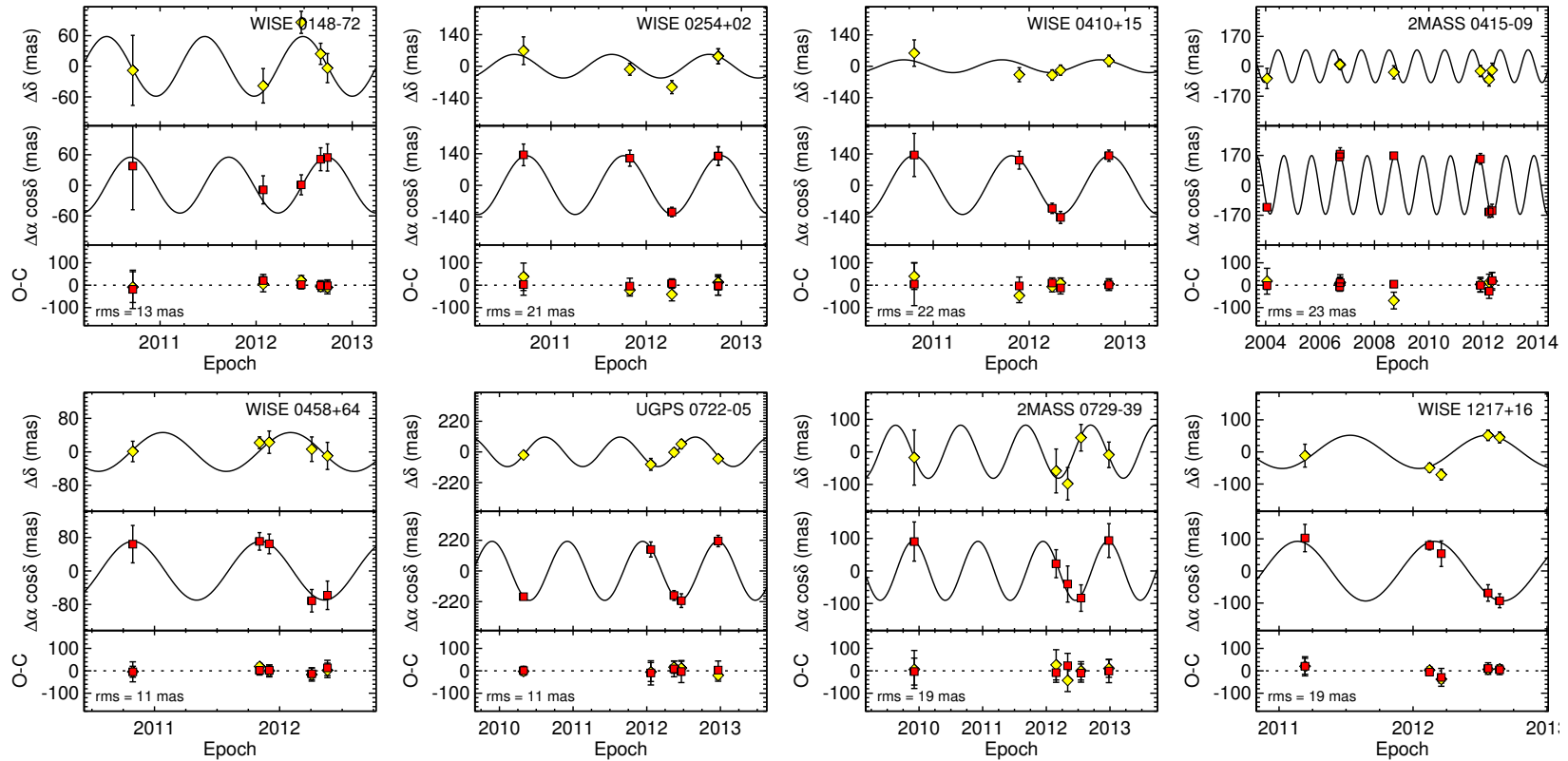


Figure S1: For each object, the top and middle panels show relative astrometry in  $\delta$  and  $\alpha$ , respectively, as a function of Julian year after subtracting the best-fit proper motion. (This is for display purposes only; in our analysis we fit for both the proper motion and parallax simultaneously.) The bottom panels show the residuals after subtracting both the parallax and proper motion and give the rms of the data about the fit.

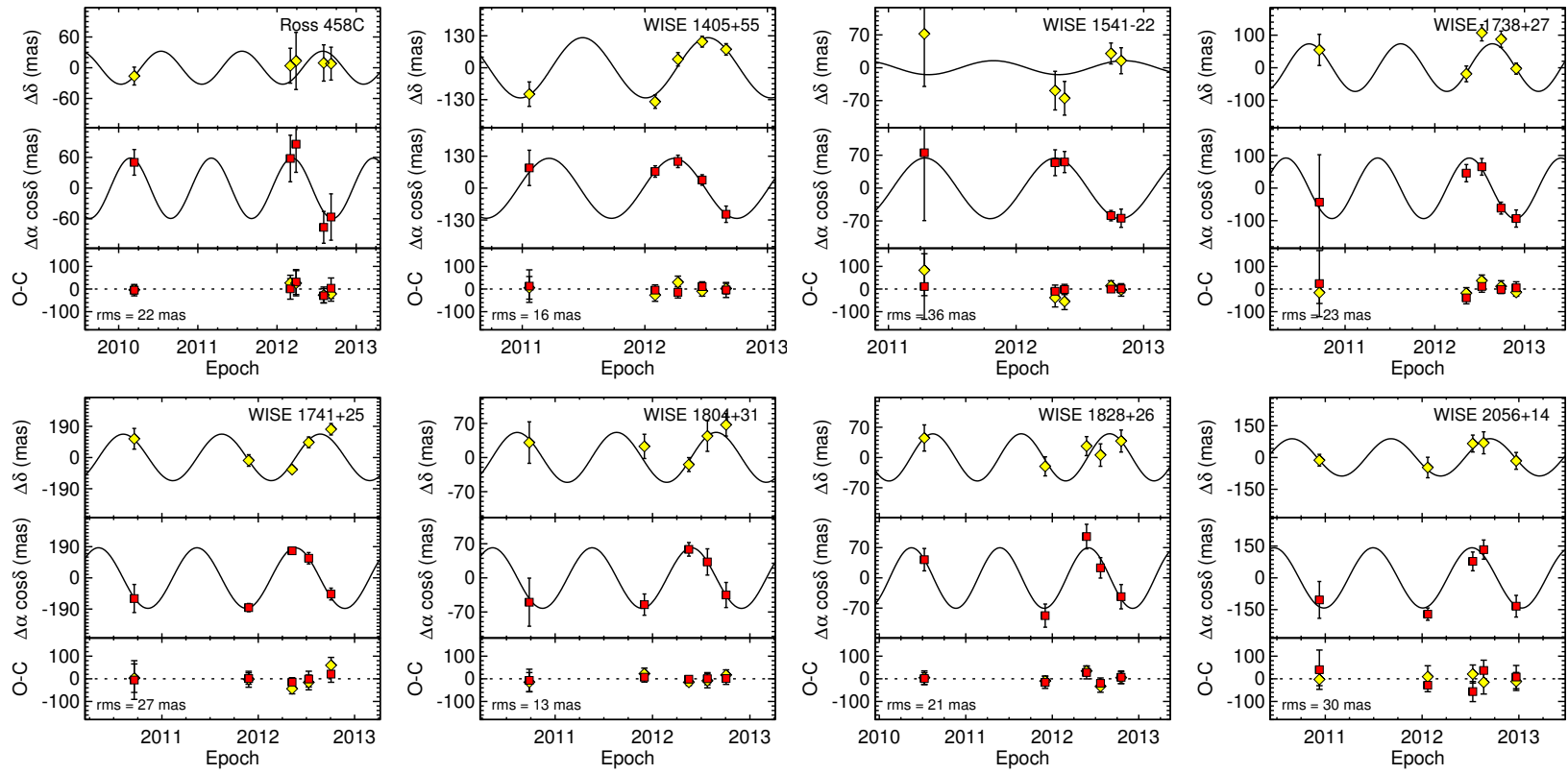


Figure S1: (Continued)



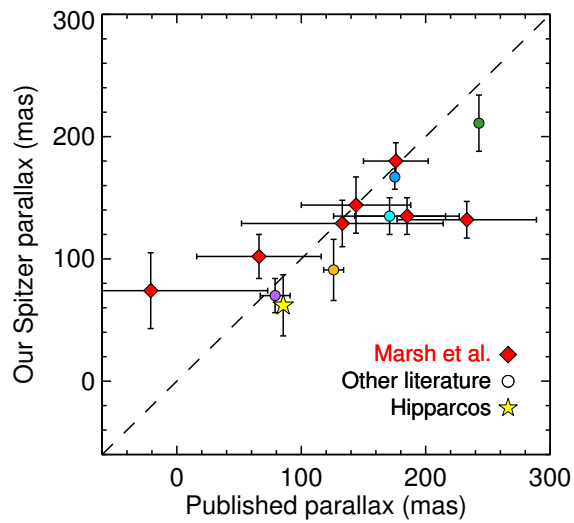


Figure S2: Comparison of our *Spitzer* parallaxes to published values. The largest single comparison sample are seven of our science targets that also have parallaxes from (35), shown as red diamonds. We also observed a control sample of five late-T dwarfs that had previously published parallaxes. The  $\chi^2$  computed from the differences between our parallaxes and published values is reasonable for both our control sample ( $\chi^2 = 5.7$ , 5 dof) and the Marsh et al. sample ( $\chi^2 = 5.7$ , 7 dof).

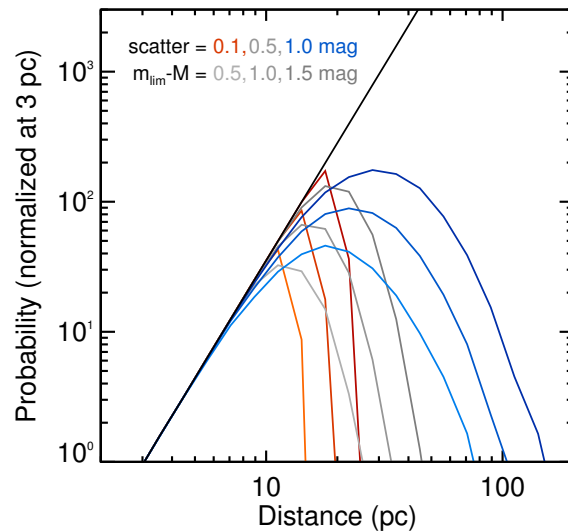


Figure S3: Distance priors assuming objects are uniformly distributed in volume (straight black line) or discovered in a magnitude limited survey (colored/gray lines). These simulations assume a single class of objects that have a mean absolute magnitude  $M$  and intrinsic scatter of 0.1 mag (red/orange), 0.5 mag (gray), or 1.0 mag (blue). We consider limiting magnitudes ( $m_{\text{lim}}$ ) that are 0.5 mag, 1.0 mag, or 1.5 mag fainter than the mean absolute magnitude of the objects, and the resulting distance distributions are normalized to unity at 3 pc. This shows that a prior uniform in volume is not appropriate for the vast majority of objects discovered in a magnitude limited survey as only the very nearest objects follow such a distribution. Most objects would be discovered near the peaks of these probability distributions, and thus a flat prior in distance and parallax would be more reasonable. Since we do not know the absolute magnitudes of Y dwarfs a priori, we conservatively assume a flat prior in parallax in our astrometric analysis.

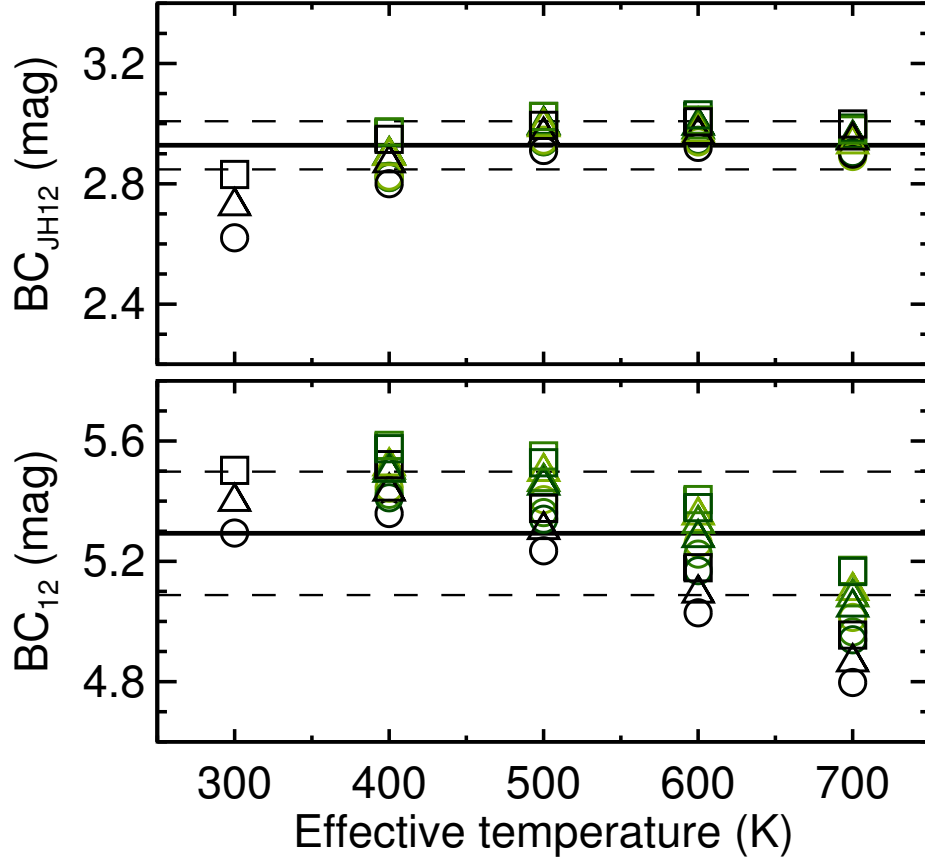


Figure S4: Bolometric corrections derived from model atmospheres (11, 15) for the super-magnitudes  $m_{JH12}$  (top) and  $m_{12}$  (bottom). The mean for each set of models is shown as a solid line, with dashed lines showing  $\pm 1\sigma$  uncertainty from the rms. We used models with surface gravities of  $10^4 \text{ cm s}^{-2}$  (circles),  $3 \times 10^4 \text{ cm s}^{-2}$  (triangles), and  $10^5 \text{ cm s}^{-2}$  (squares). The shades of symbols indicate either cloud-free models (black) or  $f_{\text{sed}} = 3, 4, \text{ or } 5$  (light, medium, and dark green, respectively), with larger  $f_{\text{sed}}$  corresponding to thinner clouds. The very weak dependence of these bolometric corrections on effective temperature enables us to adopt a single value for each super-magnitude for our entire sample of late-T and Y dwarfs.

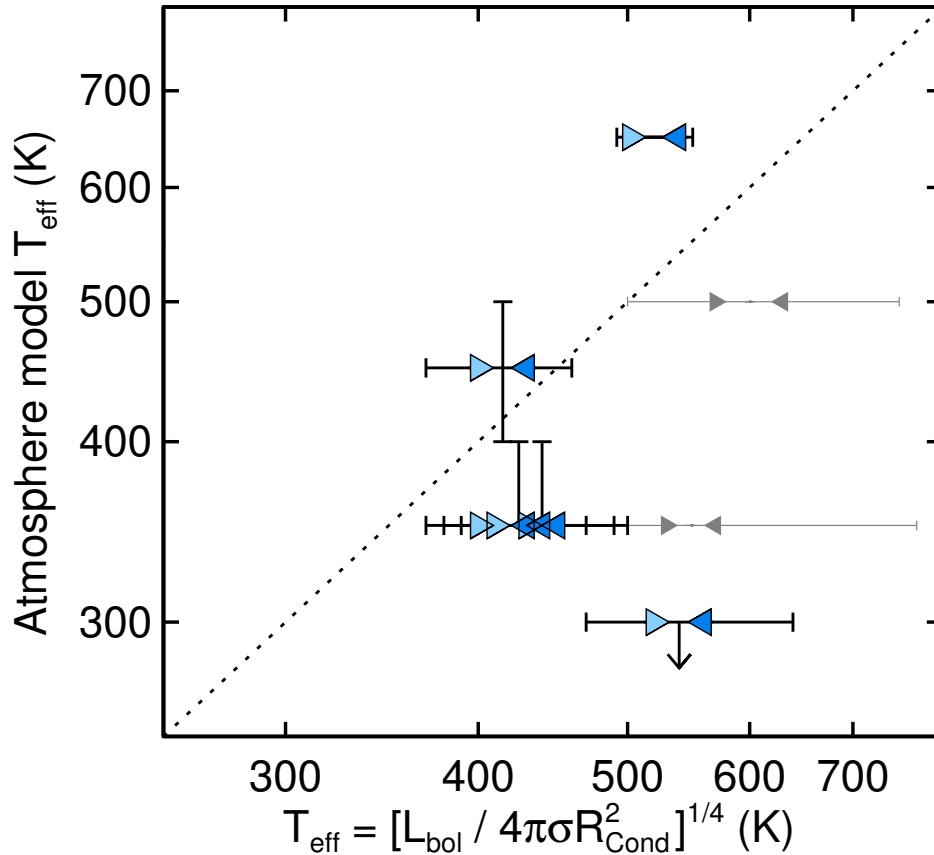


Figure S5: Effective temperatures estimated from model atmosphere fitting (3) plotted as a function of our luminosity-based  $T_{\text{eff}}$  estimates. Symbols are the same as in Fig. 4, with triangles showing the  $T_{\text{eff}}$  at ages of 1 Gyr and 5 Gyr and  $x$ -axis error bars indicating the uncertainty due to luminosity errors. Objects with very uncertain  $L_{\text{bol}}$  are shown in gray. We plot the best-fit model atmosphere  $T_{\text{eff}}$  with error bars showing the range of model parameters consistent with the data reported in Table 6 of (3). We find that the Y dwarfs with model atmosphere temperatures of 350 K are in fact significantly warmer ( $\approx 400$ – $500$  K). The most extreme case is WISEP J1828+2650 ( $\geq Y2$ ) for which model atmospheres give an upper limit of  $\leq 300$  K (3), and we find  $\approx 450$ – $650$  K. WISEP J0410+1502 is the only Y dwarf for which model atmospheres predict a  $T_{\text{eff}}$  in agreement with our values, but this is also the lowest gravity model atmosphere fit ( $\log g = 3.75$ ) that would imply a young age and mass of only  $3 M_{\text{Jup}}$ . UGPS J0722–0540 (T9) has a best-fit model atmosphere  $T_{\text{eff}}$  of 650 K, much warmer than our luminosity-based estimate of  $\approx 500$ – $550$  K.

Table S1. Parallax and Proper Motion MCMC Results

| Target                             | $\pi_{\text{rel}}$<br>(") | $\alpha_{J2000}$<br>(deg) | $\delta_{J2000}$<br>(deg) | Epoch<br>(MJD) | $\mu_{\alpha} \cos \delta$<br>(" year <sup>-1</sup> ) | $\mu_{\delta}$<br>(" year <sup>-1</sup> ) | $\mu$<br>(" year <sup>-1</sup> ) | P.A.<br>(deg) | $\chi^2/\text{dof}$ | $N_{\text{ep}}$ | $\Delta t$<br>(yr) | $N_{\text{ref}}$ | $N_{\text{cal}}$ |
|------------------------------------|---------------------------|---------------------------|---------------------------|----------------|---|---|----------------------------------|---------------|---------------------|-----------------|--------------------|------------------|------------------|
| WISEP J014807.25–720258.8          | 0.060(16)                 | 027.03049                 | –72.04965                 | 55458.49       | 1.257(38)   | –0.008(33)                                | 1.257(38)                        | 90.4 ± 1.5    | 1.9/5               | 5               | 2.03               | 207              | 27               |
| PSO J043.5395+02.3995 <sup>a</sup> | 0.135(15)                 | 043.53988                 | +02.39964                 | 55456.99       | 2.588(27)   | 0.273(27)                                 | 2.602(27)                        | 84.0 ± 0.6    | 3.3/3               | 4               | 2.04               | 100              | 19               |
| WISEP J041022.71+150248.5          | 0.132(15)                 | 062.59494                 | +15.04641                 | 55490.07       | 0.958(37)   | –2.229(29)                                | 2.426(30)                        | 156.7 ± 0.9   | 3.4/5               | 5               | 2.03               | 154              | 19               |
| 2MASS J0415195–093506              | 0.167(10)                 | 063.83469                 | –09.58437                 | 53024.06       | 2.204(3)  | 0.541(46)                                 | 2.269(3)                         | 76.21 ± 0.11  | 5.5/9               | 7               | 8.27               | 75               | 17               |
| WISEP J045853.90+643451.9          | 0.070(19)                 | 074.72478                 | +64.58131                 | 55498.85       | 0.136(45)   | 0.317(22)                                 | 0.347(26)                        | 23 ± 7        | 2.7/5               | 5               | 1.56               | 124              | 28               |
| UGPS J072227.51–054031.2           | 0.211(23)                 | 110.61371                 | –05.67496                 | 55316.49       | –0.893(16)  | 0.349(10)                                 | 0.959(15)                        | 291.3 ± 0.7   | 1.3/5               | 5               | 2.64               | 84               | 46               |
| 2MASS J07290002–3954043            | 0.091(25)                 | 112.24794                 | –39.89626                 | 55169.61       | –0.540(25)  | 1.694(30)                                 | 1.778(30)                        | 342.3 ± 0.8   | 1.2/5               | 5               | 3.06               | 105              | 60               |
| WISEP J121756.91+162640.2          | 0.099(16)                 | 184.48726                 | +16.44439                 | 55632.99       | 0.786(42)   | –1.224(27)                                | 1.455(38)                        | 147.3 ± 1.3   | 7.0/5               | 5               | 1.45               | 103              | 8                |
| Ross 458C                          | 0.062(25)                 | 195.17351                 | +12.35406                 | 55268.87       | –0.649(20)  | –0.045(12)                                | 0.650(20)                        | 266.1 ± 1.1   | 3.2/5               | 5               | 2.49               | 62               | 11               |
| WISEP J140518.40+553421.5          | 0.129(19)                 | 211.32589                 | +55.57258                 | 55583.18       | –2.263(47)  | 0.288(41)                                 | 2.281(48)                        | 277.3 ± 1.0   | 3.0/5               | 5               | 1.61               | 131              | 17               |
| WISEP J154151.65–225025.2          | 0.074(31)                 | 235.46470                 | –22.84053                 | 55664.92       | –0.870(130)   | –0.013(58)                                | 0.870(130)                       | 269 ± 4       | 4.3/5               | 5               | 1.54               | 216              | 40               |
| WISEP J173835.52+273258.9          | 0.102(18)                 | 264.64812                 | +27.54967                 | 55457.58       | 0.292(63)   | –0.396(22)                                | 0.493(40)                        | 144 ± 6       | 6.4/5               | 5               | 2.19               | 121              | 22               |
| WISEP J174124.26+255319.5          | 0.180(15)                 | 265.35094                 | +25.88859                 | 55457.57       | –0.509(35)  | –1.463(32)                                | 1.550(33)                        | 199.2 ± 1.3   | 7.9/5               | 5               | 2.04               | 61               | 21               |
| WISEP J180435.40+311706.1          | 0.060(11)                 | 271.14730                 | +31.28515                 | 55465.21       | –0.242(26)  | 0.017(22)                                 | 0.244(26)                        | 274 ± 5       | 2.8/5               | 5               | 2.02               | 194              | 42               |
| WISEP J182831.08+265037.8          | 0.070(14)                 | 277.12961                 | +26.84387                 | 55387.33       | 1.020(15)   | 0.173(16)                                 | 1.034(15)                        | 80.4 ± 0.9    | 6.5/5               | 5               | 2.28               | 209              | 45               |
| WISEP J205628.90+145953.3          | 0.144(23)                 | 314.12055                 | +14.99824                 | 55540.03       | 0.761(46)   | 0.500(21)                                 | 0.911(41)                        | 56.7 ± 1.9    | 4.0/5               | 5               | 2.03               | 74               | 30               |

<sup>a</sup>WISEP J025409.45+022359.1

Note. — This table gives all the astrometric parameters derived from our MCMC analysis. For parameters in units of arcseconds, errors are given in parentheses in units of milliarcsec.  $\pi_{\text{rel}}$ : The parallax relative to the reference star frame. Corrections to the absolute frame are negligible here. ( $\alpha$ ,  $\delta$ , MJD): Coordinates that correspond to the epoch listed, which is the first epoch of *Spitzer* observations for that target. ( $\mu_{\alpha} \cos \delta$ ,  $\mu_{\delta}$ ,  $\mu$ , P.A.): Proper motion parameters are listed both as the direct fitting results (i.e., in  $\alpha$  and  $\delta$ ) and the computed quantities of total amplitude ( $\mu$ ) and position angle.  $\chi^2/\text{dof}$ : The lowest  $\chi^2$  in each set of MCMC chains along with the degrees of freedom.  $N_{\text{ref}}$ : Total number of reference stars used.  $N_{\text{cal}}$ : Subset of reference stars from the *WISE* All-Sky Source Catalog used in the absolute astrometric calibration of constant and linear terms.

Table S2. Measurements of Late-T and Y dwarfs with Parallaxes

| Object                             | Spec. Type  | Distance (pc)           | Y (mag)          | J (mag)          | H (mag)          | K (mag)          | [3.6] (mag)      | [4.5] (mag)      | References    |
|------------------------------------|-------------|-------------------------|------------------|------------------|------------------|------------------|------------------|------------------|---------------|
| PSO J043.5395+02.3995 <sup>a</sup> | T8          | $7.4^{+0.9}_{-1.7}$     | ...              | $16.14 \pm 0.12$ | $16.51 \pm 0.12$ | $16.84 \pm 0.12$ | $14.67 \pm 0.02$ | $12.68 \pm 0.02$ | (0,33)        |
| 2MASS J0415195-093506              | T8          | $5.71^{+0.06}_{-0.05}$  | $16.28 \pm 0.03$ | $15.32 \pm 0.03$ | $15.70 \pm 0.03$ | $15.83 \pm 0.03$ | $14.10 \pm 0.04$ | $12.29 \pm 0.03$ | (12,54,59,64) |
| 2MASS J07290002-3954043            | T8p         | $7.9 \pm 0.5$           | $16.52 \pm 0.08$ | $15.64 \pm 0.08$ | $16.05 \pm 0.18$ | ...              | $14.47 \pm 0.01$ | $12.95 \pm 0.01$ | (12,31,50,62) |
| 2MASS J09393548-2448279            | T8          | $5.35^{+0.15}_{-0.14}$  | $16.47 \pm 0.09$ | $15.61 \pm 0.09$ | $15.96 \pm 0.09$ | $16.83 \pm 0.09$ | $13.76 \pm 0.02$ | $11.66 \pm 0.02$ | (40,54,60)    |
| 2MASSWJ1225543-273947B             | T8          | $13.3^{+0.5}_{-0.4}$    | ...              | $16.48 \pm 0.03$ | $16.91 \pm 0.03$ | $17.10 \pm 0.03$ | ...              | ...              | (12,66)       |
| Ross 458C                          | T8          | $11.70^{+0.21}_{-0.20}$ | $17.54 \pm 0.02$ | $16.71 \pm 0.01$ | $17.07 \pm 0.03$ | $16.96 \pm 0.03$ | $15.28 \pm 0.01$ | $13.77 \pm 0.01$ | (3,34,57)     |
| BD+01 2920B                        | T8p         | $17.18 \pm 0.15$        | $19.69 \pm 0.05$ | $18.71 \pm 0.05$ | $19.14 \pm 0.20$ | $19.89 \pm 0.33$ | $16.77 \pm 0.03$ | $14.71 \pm 0.01$ | (34,47)       |
| ULAS J003402.77-005206.7           | T8.5        | $14.56^{+0.30}_{-0.29}$ | $18.90 \pm 0.10$ | $18.15 \pm 0.03$ | $18.49 \pm 0.04$ | $18.48 \pm 0.05$ | $16.28 \pm 0.03$ | $14.49 \pm 0.03$ | (3,12,68)     |
| CFBDS J005910.90-011401.3          | T8.5        | $9.69^{+0.20}_{-0.19}$  | $18.82 \pm 0.02$ | $18.06 \pm 0.03$ | $18.27 \pm 0.05$ | $18.69 \pm 0.05$ | $15.71 \pm 0.01$ | $13.66 \pm 0.01$ | (3,12,50,58)  |
| WISEP J045853.90+643451.9A         | T8.5        | $14^{+5}_{-3}$          | ...              | $17.50 \pm 0.07$ | $17.77 \pm 0.11$ | ...              | ...              | ...              | (0,55)        |
| WISE J11838.70+312537.9            | T8.5        | $8.29 \pm 0.15$         | $19.18 \pm 0.12$ | $17.79 \pm 0.05$ | $18.15 \pm 0.06$ | ...              | $15.60 \pm 0.03$ | $13.37 \pm 0.02$ | (48)          |
| ULAS J133553.45+113005.2           | T8.5        | $10.01 \pm 0.16$        | $18.81 \pm 0.04$ | $17.90 \pm 0.01$ | $18.25 \pm 0.01$ | $18.28 \pm 0.03$ | $15.95 \pm 0.03$ | $13.91 \pm 0.03$ | (3,12,56)     |
| Wolf 940B                          | T8.5        | $11.9^{+0.6}_{-0.5}$    | $18.97 \pm 0.04$ | $18.18 \pm 0.03$ | $18.77 \pm 0.03$ | $18.97 \pm 0.06$ | $16.44 \pm 0.03$ | $14.43 \pm 0.03$ | (3,46,61,67)  |
| UGPS J072227.51-054031.2           | T9          | $4.12 \pm 0.04$         | $17.37 \pm 0.02$ | $16.52 \pm 0.02$ | $16.90 \pm 0.02$ | $17.07 \pm 0.08$ | $14.28 \pm 0.05$ | $12.19 \pm 0.04$ | (3,32,63)     |
| WISEP J121756.91+162640.2A         | T9          | $10.1^{+1.9}_{-1.4}$    | $18.59 \pm 0.04$ | $17.98 \pm 0.02$ | $18.31 \pm 0.05$ | $18.94 \pm 0.04$ | ...              | ...              | (0,10)        |
| CFBDSIR J145829+101343A            | T9          | $31.9^{+2.8}_{-2.4}$    | $20.81 \pm 0.21$ | $19.83 \pm 0.02$ | $20.18 \pm 0.10$ | $20.63 \pm 0.24$ | ...              | ...              | (2,10,12)     |
| WISEP J174124.26+255319.5          | T9          | $5.6^{+0.5}_{-0.4}$     | $17.23 \pm 0.02$ | $16.18 \pm 0.02$ | $16.31 \pm 0.04$ | $17.02 \pm 0.20$ | $14.43 \pm 0.02$ | $12.39 \pm 0.02$ | (0,7)         |
| WISEP J014807.25-720258.8          | T9.5        | $17^{+6}_{-4}$          | ...              | $18.96 \pm 0.07$ | $19.22 \pm 0.04$ | ...              | $16.84 \pm 0.05$ | $14.65 \pm 0.02$ | (0,3,7)       |
| WISEP J045853.90+643451.9B         | T9.5        | $14^{+5}_{-3}$          | ...              | $18.48 \pm 0.07$ | $18.79 \pm 0.11$ | ...              | ...              | ...              | (0,55)        |
| WISEP J180435.40+311706.1          | T9.5:       | $16.7^{+3.7}_{-2.6}$    | ...              | $18.70 \pm 0.05$ | $19.21 \pm 0.11$ | ...              | $16.62 \pm 0.04$ | $14.60 \pm 0.02$ | (0,7)         |
| WISE J035934.06-540154.6           | Y0          | $5.9^{+1.3}_{-0.8}$     | ...              | $21.56 \pm 0.24$ | $22.20 \pm 0.43$ | ...              | $17.55 \pm 0.07$ | $15.33 \pm 0.02$ | (8,35)        |
| WISEP J041022.71+150248.5          | Y0          | $7.6^{+1.0}_{-0.8}$     | $19.61 \pm 0.04$ | $19.44 \pm 0.03$ | $20.02 \pm 0.05$ | $19.91 \pm 0.07$ | $16.56 \pm 0.01$ | $14.12 \pm 0.01$ | (0,3,9)       |
| WISEP J121756.91+162640.2B         | Y0          | $10.1^{+1.9}_{-1.4}$    | $20.26 \pm 0.04$ | $20.08 \pm 0.03$ | $20.51 \pm 0.06$ | $21.10 \pm 0.12$ | ...              | ...              | (0,10)        |
| WISEP J140518.40+553421.5          | Y0p         | $7.8^{+1.3}_{-1.0}$     | $21.24 \pm 0.10$ | $21.06 \pm 0.06$ | $21.41 \pm 0.08$ | ...              | $16.78 \pm 0.01$ | $14.02 \pm 0.01$ | (0,3,9)       |
| WISE J163940.83-684738.6           | Y0:         | $5.0^{+0.6}_{-0.5}$     | ...              | $20.76 \pm 0.08$ | ...              | ...              | ...              | ...              | (53)          |
| WISEP J173835.52+273258.9          | Y0          | $9.8^{+2.1}_{-1.5}$     | $19.86 \pm 0.08$ | $20.05 \pm 0.09$ | $20.45 \pm 0.09$ | $20.58 \pm 0.10$ | $16.87 \pm 0.01$ | $14.42 \pm 0.01$ | (0,3,9)       |
| WISEP J205628.90+145953.3          | Y0          | $6.9^{+1.3}_{-1.0}$     | $19.77 \pm 0.06$ | $19.43 \pm 0.04$ | $19.96 \pm 0.04$ | $20.01 \pm 0.06$ | $15.90 \pm 0.01$ | $13.89 \pm 0.01$ | (0,3,9)       |
| WISEP J154151.65-225025.2          | Y0.5        | $14^{+10}_{-4}$         | $21.46 \pm 0.13$ | $21.12 \pm 0.06$ | $22.17 \pm 0.25$ | ...              | $16.92 \pm 0.02$ | $14.12 \pm 0.01$ | (0,8,9)       |
| WISE J035000.32-565830.2           | Y1          | $3.7^{+1.6}_{-0.4}$     | ...              | ...              | ...              | ...              | $17.94 \pm 0.10$ | $14.69 \pm 0.02$ | (8,35)        |
| WISE J053516.80-750024.9           | $\geq Y1$ : | $21^{+13}_{-11}$        | ...              | ...              | ...              | ...              | $17.77 \pm 0.09$ | $15.01 \pm 0.02$ | (8,35)        |
| WISEP J182831.08+265037.8          | $\geq Y2$   | $14.3^{+3.6}_{-2.4}$    | $23.03 \pm 0.17$ | $23.48 \pm 0.23$ | $22.85 \pm 0.24$ | $23.48 \pm 0.36$ | $16.84 \pm 0.01$ | $14.27 \pm 0.01$ | (0,8,9)       |
| CFBDSIR J145829+101343B            | ...         | $31.9^{+2.8}_{-2.4}$    | $22.36 \pm 0.24$ | $21.85 \pm 0.06$ | $22.51 \pm 0.16$ | $22.83 \pm 0.30$ | ...              | ...              | (10,12)       |
| WD 0806-661B                       | ...         | $19.2 \pm 0.6$          | ...              | ...              | ...              | ...              | $19.65 \pm 0.15$ | $16.88 \pm 0.05$ | (25,65)       |

<sup>a</sup>WISEP J025409.45+022359.1

Note. — Compilation of distances, spectral types, and apparent magnitudes for all objects of spectral type T8 or later with parallax measurements. Uncertainties in spectral types are 0.5 subtypes unless otherwise noted ( $\pm 1$  subtype errors are denoted by “:”). All near-IR photometry is on the MKO system. Reference numbers correspond to the citations in the main article, with (0) referring to the work presented here.

Table S3. Mean Absolute Magnitudes of Normal Late-T and Y Dwarfs

| Spec.<br>Type | Y     |                       |                       |     | J     |                       |                       |     | H     |                       |                       |     | K     |                       |                       |     | [3.6] |                       |                       |     | [4.5] |                       |                       |     |
|---------------|-------|-----------------------|-----------------------|-----|-------|-----------------------|-----------------------|-----|-------|-----------------------|-----------------------|-----|-------|-----------------------|-----------------------|-----|-------|-----------------------|-----------------------|-----|-------|-----------------------|-----------------------|-----|
|               | avg   | $\sigma_{\text{avg}}$ | $\sigma_{\text{add}}$ | $n$ | avg   | $\sigma_{\text{avg}}$ | $\sigma_{\text{add}}$ | $n$ | avg   | $\sigma_{\text{avg}}$ | $\sigma_{\text{add}}$ | $n$ | avg   | $\sigma_{\text{avg}}$ | $\sigma_{\text{add}}$ | $n$ | avg   | $\sigma_{\text{avg}}$ | $\sigma_{\text{add}}$ | $n$ | avg   | $\sigma_{\text{avg}}$ | $\sigma_{\text{add}}$ | $n$ |
| T8.0          | 17.40 | 0.03                  | $\geq 0.25$           | 3   | 16.43 | 0.02                  | $\geq 0.46$           | 5   | 16.82 | 0.03                  | $\geq 0.43$           | 5   | 16.93 | 0.03                  | $\geq 0.80$           | 5   | 15.11 | 0.03                  | $\geq 0.15$           | 4   | 13.40 | 0.02                  | $\geq 0.21$           | 4   |
| T8.5          | 18.81 | 0.03                  | $\geq 0.51$           | 5   | 17.87 | 0.02                  | $\geq 0.44$           | 6   | 18.20 | 0.03                  | $\geq 0.45$           | 6   | 18.27 | 0.03                  | $\geq 0.40$           | 4   | 15.83 | 0.02                  | $\geq 0.22$           | 5   | 13.79 | 0.02                  | $\geq 0.12$           | 5   |
| T9.0          | 19.26 | 0.03                  | $\geq 0.88$           | 4   | 18.39 | 0.03                  | $\geq 0.95$           | 4   | 18.77 | 0.03                  | $\geq 1.08$           | 4   | 18.89 | 0.08                  | $\geq 0.57$           | 4   | 16.17 | 0.05                  | $\geq 0.23$           | 2   | 14.09 | 0.04                  | $\geq 0.20$           | 2   |
| T9.5          | ...   | ...                   | ...                   | 0   | 17.68 | 0.33                  | $\leq 0.37$           | 3   | 18.08 | 0.33                  | $\leq 0.39$           | 3   | ...   | ...                   | ...                   | 0   | 15.58 | 0.37                  | $\leq 0.41$           | 2   | 13.51 | 0.37                  | $\leq 0.43$           | 2   |
| Y0.0          | 20.24 | 0.17                  | $\leq 0.17$           | 4   | 20.09 | 0.17                  | $\leq 0.25$           | 4   | 20.60 | 0.17                  | $\leq 0.25$           | 4   | 20.70 | 0.18                  | $\leq 0.16$           | 4   | 16.99 | 0.19                  | $\leq 0.21$           | 3   | 14.66 | 0.19                  | $\leq 0.28$           | 3   |

Note. — For each spectral type and bandpass four numbers are given: (1) the weighted mean absolute magnitude (“avg”); (2) error on the weighted mean ( $\sigma_{\text{avg}}$ ); (3) the additional scatter ( $\sigma_{\text{add}}$ ) needed to make  $p(\chi^2) = 0.5$ ; and (4) the number of objects from Table S2 used in the bin ( $n$ ). For cases where the rms is larger than can be explained by measurement error, i.e.,  $p(\chi^2) < 0.5$ , the  $\sigma_{\text{add}}$  values are essentially lower limits on the amount of intrinsic scatter in the absolute magnitudes at that spectral type. For cases where the rms can be explained simply by measurement uncertainties, i.e.,  $p(\chi^2) \geq 0.5$ , the  $\sigma_{\text{add}}$  values represent the upper limit on the amount of additional intrinsic scatter that could be tolerated while still keeping  $p(\chi^2) \geq 0.5$ . Only “normal” objects are used for these averages, i.e., excluding objects typed as peculiar (2MASS J0729–3954, BD+01 2920B, and WISEP J1405+5534) and two Y0 dwarfs with very uncertain or preliminary distances (WISE J0359–5401 and WISE J1639–6847).

Table S4. Bolometric Corrections

| Spec. Type | $YJH$<br>(mag) | $YJ$<br>(mag) | $JH$<br>(mag) | $Y$<br>(mag) | $J$<br>(mag) | $H$<br>(mag) |
|------------|----------------|---------------|---------------|--------------|--------------|--------------|
| T8.0       | 2.0            | 2.0           | 2.3           | 1.6          | 2.4          | 2.1          |
| T8.5       | 1.6            | 1.6           | 1.9           | 1.1          | 2.0          | 1.6          |
| T9.0       | 1.6            | 1.5           | 1.9           | 1.0          | 2.0          | 1.7          |
| T9.5       | ...            | ...           | 1.8           | ...          | 1.9          | 1.5          |
| Y0.0       | 0.8            | 0.9           | 0.7           | 0.8          | 0.9          | 0.4          |
| Y0.5       | -0.7           | -0.6          | -0.7          | -0.7         | -0.4         | -1.5         |

Note. — These bolometric corrections were derived from single objects with photometry in at least  $J$ ,  $H$ , [3.6], and [4.5] bands, i.e., capturing  $\gtrsim 50\%$  of the bolometric flux. We used model atmospheres (*I2*, *I3*) to compute their bolometric magnitudes and thereby bolometric corrections in near-IR bands:  $BC_X = m_{\text{bol}} - m_X$ . The values listed here are the weighted averages of values derived for individual objects in each spectral type bin. The rms about these weighted averages was 0.6 mag, so we take this as the uncertainty in these bolometric corrections.



Table S5. Derived Properties of Late-T and Y dwarfs with Parallaxes

| Object                    | Spec. Type | $m_{\text{bol}}$ (mag) | $\log(L_{\text{bol}}/L_{\odot})$        | Cond ( $t = 1$ Gyr)                            |  |                                      |  | Cond ( $t = 5$ Gyr)                            |  |  |  |
|---------------------------|------------|------------------------|---|--|--|--------------------------------------|--|--|--|--|--|
|                           |            |                        |   | $T_{\text{eff}}$ (K)                           | $R_{\star}$ ( $R_{\text{Jup}}$ )                       | $M_{\star}$ ( $M_{\text{Jup}}$ )     | $\log g$ (cgs)                         | $T_{\text{eff}}$ (K)                           | $R_{\star}$ ( $R_{\text{Jup}}$ )                       | $M_{\star}$ ( $M_{\text{Jup}}$ )                 | $\log g$ (cgs)                           |
| PSO J043.5395+02.3995     | T8         | 18.48 ± 0.09           | -5.75 <sup>+0.11</sup> <sub>-0.10</sub> | 660 ± 40                                       | 0.983 <sup>+0.007</sup> <sub>-0.006</sub>              | 17.0 <sup>+1.7</sup> <sub>-1.5</sub> | 4.63 ± 0.05                            | 720 <sup>+50</sup> <sub>-40</sub>              | 0.830 ± 0.012  | 39 <sup>+4</sup> <sub>-3</sub>                   | 5.14 ± 0.05                              |
| 2MASS J0415195-093506     | T8         | 17.85 ± 0.08           | -5.72 ± 0.03                            | 673 <sup>+14</sup> <sub>-13</sub>              | 0.9820 ± 0.0017  | 17.4 ± 0.5                           | 4.64 ± 0.01                            | 734 ± 16                                       | 0.827 ± 0.004  | 40.1 <sup>+1.2</sup> <sub>-1.1</sub>             | 5.15 ± 0.01                              |
| 2MASS J07290002-3954043   | T8p        | 18.28 ± 0.09           | -5.61 ± 0.07                            | 720 ± 30                                       | 0.976 ± 0.003  | 19.2 <sup>+1.2</sup> <sub>-1.1</sub> | 4.69 ± 0.03                            | 790 ± 30                                       | 0.815 <sup>+0.006</sup> <sub>-0.007</sub>              | 43.7 <sup>+2.1</sup> <sub>-2.0</sub>             | 5.20 ± 0.03                              |
| 2MASS J09393548-2448279   | T8         | 17.68 ± 0.08           | -5.71 ± 0.04                            | 678 <sup>+17</sup> <sub>-16</sub>              | 0.981 ± 0.002  | 17.6 ± 0.6                           | 4.64 <sup>+0.01</sup> <sub>-0.01</sub> | 740 <sup>+20</sup> <sub>-19</sub>              | 0.825 ± 0.005  | 40.5 ± 1.4                                       | 5.16 ± 0.02                              |
| 2MASSWJ1225543-273947B    | T8         | 18.9 ± 0.6             | -5.41 ± 0.23                            | 810 <sup>+130</sup> <sub>-110</sub>            | 0.962 <sup>+0.016</sup> <sub>-0.022</sub>              | 23 <sup>+5</sup> <sub>-4</sub>       | 4.79 ± 0.11                            | 890 <sup>+140</sup> <sub>-120</sub>            | 0.80 ± 0.02  | 50 <sup>+8</sup> <sub>-7</sub>                   | 5.28 ± 0.09                              |
| Ross 458C                 | T8         | 19.24 ± 0.08           | -5.66 ± 0.04                            | 649 ± 14 <sup>a</sup>                          | 1.142 ± 0.004 <sup>a</sup>                             | 6.8 ± 0.3 <sup>a</sup>               | 4.10 ± 0.02 <sup>a</sup>               | 692 ± 16 <sup>a</sup>                          | 1.006 <sup>+0.006 a</sup> <sub>-0.005</sub>            | 15.9 <sup>+0.6 a</sup> <sub>-0.9</sub>           | 4.58 <sup>+0.02 a</sup> <sub>-0.03</sub> |
| BD+01 2920B               | T8p        | 20.75 ± 0.08           | -5.93 ± 0.03                            | 592 ± 14                                       | 1.008 ± 0.008  | 13.4 <sup>+0.9</sup> <sub>-0.8</sub> | 4.50 ± 0.03                            | 644 <sup>+15</sup> <sub>-15</sub>              | 0.851 ± 0.004  | 33.8 ± 1.0                                       | 5.05 ± 0.01                              |
| ULAS J003402.77-005206.7  | T8.5       | 20.35 ± 0.08           | -5.91 ± 0.04                            | 598 <sup>+16</sup> <sub>-15</sub>              | 1.004 ± 0.009  | 13.8 <sup>+1.0</sup> <sub>-0.9</sub> | 4.52 ± 0.04                            | 651 <sup>+16</sup> <sub>-15</sub>              | 0.849 ± 0.004  | 34.2 ± 1.1                                       | 5.06 ± 0.01                              |
| CFBDS J005910.90-011401.3 | T8.5       | 19.80 ± 0.08           | -6.04 ± 0.04                            | 550 ± 12                                       | 1.0170 ± 0.0005  | 11.9 ± 0.3                           | 4.44 ± 0.01                            | 596 ± 14                                       | 0.865 ± 0.005  | 30.4 <sup>+1.1</sup> <sub>-1.1</sub>             | 4.99 ± 0.02                              |
| WISE J045853.90+643451.9A | T8.5       | 19.5 ± 0.6             | -5.6 <sup>+0.4</sup> <sub>-0.3</sub>    | 730 <sup>+180</sup> <sub>-130</sub>            | 0.98 ± 0.03  | 20 <sup>+8</sup> <sub>-6</sub>       | 4.70 <sup>+0.17</sup> <sub>-0.18</sub> | 800 <sup>+200</sup> <sub>-150</sub>            | 0.81 <sup>+0.04</sup> <sub>-0.03</sub>                 | 44 <sup>+12</sup> <sub>-10</sub>                 | 5.21 <sup>+0.14</sup> <sub>-0.15</sub>   |
| WISE J11838.70+312537.9   | T8.5       | 19.56 ± 0.08           | -6.08 ± 0.04                            | 538 ± 11                                       | 1.0176 ± 0.0005  | 11.6 ± 0.3                           | 4.43 ± 0.01                            | 582 ± 14                                       | 0.870 ± 0.005  | 29.2 ± 1.1                                       | 4.97 ± 0.02                              |
| ULAS J133553.45+113005.2  | T8.5       | 19.93 ± 0.08           | -6.07 ± 0.04                            | 542 ± 11                                       | 1.0174 ± 0.0005  | 11.7 ± 0.3                           | 4.43 ± 0.01                            | 587 <sup>+14</sup> <sub>-13</sub>              | 0.869 ± 0.005  | 29.6 ± 1.1                                       | 4.97 ± 0.02                              |
| Wolf 940B                 | T8.5       | 20.39 ± 0.08           | -6.10 ± 0.05                            | 532 <sup>+17</sup> <sub>-16</sub>              | 1.0178 <sup>+0.0007</sup> <sub>-0.0008</sub>           | 11.5 ± 0.4                           | 4.42 ± 0.01                            | 575 <sup>+20</sup> <sub>-19</sub>              | 0.873 ± 0.007  | 28.6 <sup>+1.6</sup> <sub>-1.5</sub>             | 4.96 ± 0.03                              |
| UGPS J072227.51-054031.2  | T9         | 18.33 ± 0.08           | -6.20 ± 0.03                            | 502 ± 10                                       | 1.0192 ± 0.0005  | 10.7 ± 0.2                           | 4.39 ± 0.01                            | 539 ± 12                                       | 0.886 ± 0.005  | 25.8 ± 0.9                                       | 4.90 ± 0.01                              |
| WISE J121756.91+162640.2A | T9         | 19.9 ± 0.6             | -6.04 <sup>+0.29</sup> <sub>-0.28</sub> | 550 <sup>+110</sup> <sub>-80</sub>             | 1.017 <sup>+0.011</sup> <sub>-0.034</sub>              | 12 <sup>+5</sup> <sub>-2</sub>       | 4.44 <sup>+0.19</sup> <sub>-0.11</sub> | 600 <sup>+120</sup> <sub>-100</sub>            | 0.86 ± 0.04  | 31 <sup>+9</sup> <sub>-8</sub>                   | 4.99 <sup>+0.15</sup> <sub>-0.16</sub>   |
| CFBDSIR J145829+101343A   | T9         | 21.8 ± 0.6             | -5.82 ± 0.26                            | 630 <sup>+110</sup> <sub>-100</sub>            | 0.987 <sup>+0.030</sup> <sub>-0.013</sub>              | 16 ± 4                               | 4.60 <sup>+0.12</sup> <sub>-0.17</sub> | 690 <sup>+120</sup> <sub>-110</sub>            | 0.84 ± 0.03  | 37 ± 8   | 5.10 <sup>+0.12</sup> <sub>-0.13</sub>   |
| WISE J174124.26+255319.5  | T9         | 18.30 ± 0.08           | -6.93 ± 0.08                            | 590 ± 30                                       | 1.009 ± 0.008  | 13.3 <sup>+2.2</sup> <sub>-1.1</sub> | 4.50 <sup>+0.08</sup> <sub>-0.04</sub> | 640 <sup>+40</sup> <sub>-30</sub>              | 0.851 <sup>+0.009</sup> <sub>-0.010</sub>              | 34 ± 2   | 5.05 ± 0.04                              |
| WISE J014807.25-720258.8  | T9.5       | 20.79 ± 0.08           | -5.97 <sup>+0.27</sup> <sub>-0.21</sub> | 570 <sup>+110</sup> <sub>-70</sub>             | 1.016 <sup>+0.019</sup> <sub>-0.035</sub>              | 12.5 <sup>+5.3</sup> <sub>-1.6</sub> | 4.47 <sup>+0.19</sup> <sub>-0.07</sub> | 630 <sup>+120</sup> <sub>-80</sub>             | 0.86 ± 0.03  | 33 <sup>+8</sup> <sub>-6</sub>                   | 5.03 <sup>+0.14</sup> <sub>-0.11</sub>   |
| WISE J045853.90+643451.9B | T9.5       | 20.4 ± 0.6             | -5.9 <sup>+0.4</sup> <sub>-0.3</sub>    | 590 <sup>+150</sup> <sub>-100</sub>            | 1.009 <sup>+0.011</sup> <sub>-0.035</sub>              | 13 <sup>+7</sup> <sub>-3</sub>       | 4.50 <sup>+0.21</sup> <sub>-0.12</sub> | 640 <sup>+170</sup> <sub>-120</sub>            | 0.85 ± 0.04  | 34 <sup>+11</sup> <sub>-9</sub>                  | 5.05 ± 0.17                              |
| WISE J180435.40+311706.1  | T9.5       | 20.67 ± 0.08           | -5.92 <sup>+0.18</sup> <sub>-0.15</sub> | 590 <sup>+70</sup> <sub>-50</sub>              | 1.007 <sup>+0.010</sup> <sub>-0.024</sub>              | 13.5 <sup>+3.6</sup> <sub>-1.8</sub> | 4.51 <sup>+0.13</sup> <sub>-0.07</sub> | 650 <sup>+80</sup> <sub>-60</sub>              | 0.850 <sup>+0.019</sup> <sub>-0.021</sub>              | 34 <sup>+6</sup> <sub>-4</sub>                   | 5.05 <sup>+0.09</sup> <sub>-0.08</sub>   |
| WISE J035934.06-540154.6  | Y0         | 21.79 ± 0.08           | -7.27 <sup>+0.18</sup> <sub>-0.13</sub> | 265 <sup>+28</sup> <sub>-19</sub>              | 1.065 ± 0.005  | 3.0 <sup>+0.8</sup> <sub>-0.5</sub>  | 3.81 <sup>+0.10</sup> <sub>-0.07</sub> | 270 <sup>+30</sup> <sub>-20</sub>              | 0.992 <sup>+0.008</sup> <sub>-0.009</sub>              | 7.9 <sup>+1.8</sup> <sub>-1.1</sub>              | 4.29 <sup>+0.10</sup> <sub>-0.07</sub>   |
| WISE J041022.71+150248.5  | Y0         | 20.53 ± 0.08           | -6.55 ± 0.08                            | 400 ± 30                                       | 1.047 ± 0.018  | 7.4 <sup>+0.8</sup> <sub>-1.0</sub>  | 4.21 <sup>+0.05</sup> <sub>-0.08</sub> | 430 ± 30                                       | 0.929 <sup>+0.010</sup> <sub>-0.011</sub>              | 17.8 <sup>+2.2</sup> <sub>-1.8</sub>             | 4.70 ± 0.06                              |
| WISE J121756.91+162640.2B | Y0         | 21.0 ± 0.6             | -6.49 <sup>+0.29</sup> <sub>-0.28</sub> | 420 <sup>+80</sup> <sub>-70</sub>              | 1.04 <sup>+0.02</sup> <sub>-0.03</sub>                 | 8 <sup>+3</sup> <sub>-2</sub>        | 4.24 <sup>+0.15</sup> <sub>-0.16</sub> | 450 <sup>+90</sup> <sub>-70</sub>              | 0.92 ± 0.04  | 19 <sup>+7</sup> <sub>-5</sub>                   | 4.73 <sup>+0.17</sup> <sub>-0.18</sub>   |
| WISE J140518.40+553421.5  | Y0p        | 20.61 ± 0.08           | -6.56 <sup>+0.14</sup> <sub>-0.12</sub> | 406 <sup>+40</sup> <sub>-30</sub>              | 1.048 <sup>+0.019</sup> <sub>-0.006</sub>              | 7.3 <sup>+1.1</sup> <sub>-1.2</sub>  | 4.21 <sup>+0.06</sup> <sub>-0.09</sub> | 430 <sup>+40</sup> <sub>-30</sub>              | 0.930 ± 0.014  | 18 <sup>+3</sup> <sub>-2</sub>                   | 4.70 ± 0.08                              |
| WISE J163940.83-684738.6  | Y0         | 21.7 ± 0.7             | -7.38 <sup>+0.27</sup> <sub>-0.27</sub> | 250 ± 40                                       | 1.061 <sup>+0.013</sup> <sub>-0.013</sub>              | 2.6 <sup>+1.2</sup> <sub>-0.7</sub>  | 3.76 <sup>+0.15</sup> <sub>-0.14</sub> | 260 <sup>+50</sup> <sub>-40</sub>              | 0.999 <sup>+0.014</sup> <sub>-0.016</sub>              | 7.0 <sup>+2.7</sup> <sub>-1.8</sub>              | 4.23 <sup>+0.16</sup> <sub>-0.13</sub>   |
| WISE J173835.52+273258.9  | Y0         | 20.87 ± 0.08           | -6.46 <sup>+0.17</sup> <sub>-0.14</sub> | 430 <sup>+50</sup> <sub>-40</sub>              | 1.043 <sup>+0.013</sup> <sub>-0.018</sub>              | 8.1 <sup>+1.8</sup> <sub>-1.2</sub>  | 4.25 <sup>+0.10</sup> <sub>-0.08</sub> | 450 <sup>+40</sup> <sub>-40</sub>              | 0.920 <sup>+0.015</sup> <sub>-0.021</sub>              | 20 <sup>+4</sup> <sub>-3</sub>                   | 4.75 <sup>+0.10</sup> <sub>-0.09</sub>   |
| WISE J205628.90+145953.3  | Y0         | 20.25 ± 0.08           | -6.52 <sup>+0.15</sup> <sub>-0.13</sub> | 410 <sup>+40</sup> <sub>-30</sub>              | 1.046 <sup>+0.019</sup> <sub>-0.012</sub>              | 7.6 <sup>+1.4</sup> <sub>-1.3</sub>  | 4.23 <sup>+0.08</sup> <sub>-0.09</sub> | 440 <sup>+50</sup> <sub>-40</sub>              | 0.925 <sup>+0.013</sup> <sub>-0.017</sub>              | 19 <sup>+3</sup> <sub>-2</sub>                   | 4.72 <sup>+0.09</sup> <sub>-0.08</sub>   |
| WISE J154151.65-225025.2  | Y0.5       | 20.72 ± 0.08           | -6.1 <sup>+0.5</sup> <sub>-0.3</sub>    | 530 <sup>+180</sup> <sub>-90</sub>             | 1.02 <sup>+0.02</sup> <sub>-0.04</sub>                 | 11 <sup>+7</sup> <sub>-3</sub>       | 4.42 <sup>+0.26</sup> <sub>-0.15</sub> | 570 <sup>+200</sup> <sub>-100</sub>            | 0.88 <sup>+0.04</sup> <sub>-0.06</sub>                 | 28 <sup>+15</sup> <sub>-8</sub>                  | 4.95 <sup>+0.24</sup> <sub>-0.17</sub>   |
| WISE J035000.32-565830.2  | Y1         | 21.05 ± 0.21           | -7.38 <sup>+0.32</sup> <sub>-0.13</sub> | 249 <sup>+49</sup> <sub>-17</sub>              | 1.060 <sup>+0.010</sup> <sub>-0.005</sub>              | 2.6 <sup>+1.4</sup> <sub>-0.4</sub>  | 3.75 <sup>+0.18</sup> <sub>-0.07</sub> | 257 <sup>+55</sup> <sub>-19</sub>              | 1.000 <sup>+0.005</sup> <sub>-0.019</sub>              | 6.9 <sup>+3.1</sup> <sub>-0.9</sub>              | 4.22 <sup>+0.18</sup> <sub>-0.06</sub>   |
| WISE J053516.80-750024.9  | ≥Y1        | 21.32 ± 0.21           | -6.0 <sup>+0.4</sup> <sub>-0.6</sub>    | 570 <sup>+170</sup> <sub>-190</sub>            | 1.02 ± 0.04  | 12 <sup>+8</sup> <sub>-6</sub>       | 4.5 ± 0.3                              | 620 <sup>+200</sup> <sub>-210</sub>            | 0.86 <sup>+0.08</sup> <sub>-0.05</sub>                 | 32 <sup>+13</sup> <sub>-16</sub>                 | 5.0 <sup>+0.2</sup> <sub>-0.4</sub>      |
| WISE J182831.08+265037.8  | ≥Y2        | 20.86 ± 0.08           | -6.13 <sup>+0.20</sup> <sub>-0.16</sub> | 520 <sup>+60</sup> <sub>-50</sub>              | 1.018 ± 0.007  | 11.2 <sup>+1.9</sup> <sub>-1.4</sub> | 4.41 <sup>+0.08</sup> <sub>-0.06</sub> | 560 <sup>+80</sup> <sub>-60</sub>              | 0.88 <sup>+0.02</sup> <sub>-0.03</sub>                 | 28 <sup>+6</sup> <sub>-4</sub>                   | 4.94 <sup>+0.11</sup> <sub>-0.09</sub>   |
| CFBDSIR J145829+101343B   | ...        | 23.0 ± 0.6             | -6.27 ± 0.26                            | 480 <sup>+80</sup> <sub>-70</sub>              | 1.023 <sup>+0.023</sup> <sub>-0.006</sub>              | 10 <sup>+2</sup> <sub>-3</sub>       | 4.36 <sup>+0.09</sup> <sub>-0.14</sub> | 520 <sup>+100</sup> <sub>-80</sub>             | 0.90 <sup>+0.03</sup> <sub>-0.04</sub>                 | 24 <sup>+7</sup> <sub>-6</sub>                   | 4.86 ± 0.15                              |
| WD 0806-661B              | ...        | 23.19 ± 0.21           | -6.81 ± 0.09                            | 350 <sup>+20</sup> <sub>-19</sub> <sup>b</sup> | 1.040 <sup>+0.009</sup> <sub>-0.008</sub> <sup>b</sup> | 6.8 ± 0.7 <sup>b</sup>               | 4.19 ± 0.05 <sup>b</sup>               | 356 <sup>+20</sup> <sub>-19</sub> <sup>b</sup> | 1.007 <sup>+0.007</sup> <sub>-0.009</sub> <sup>b</sup> | 9.0 <sup>+1.0</sup> <sub>-0.9</sub> <sup>b</sup> | 4.33 ± 0.05 <sup>b</sup>                 |

Note. — Uncertainties in spectral types are 0.5 subtypes unless otherwise noted ( $\pm 1$  subtype errors are denoted by “:”). Apparent bolometric magnitudes ( $m_{\text{bol}}$ ) and bolometric luminosities are computed as described in the text. Effective temperatures ( $T_{\text{eff}}$ ), radii ( $R_{\star}$ ), masses ( $M_{\star}$ ), and surface gravities ( $\log g$ ) are interpolated from Cond model isochrones ( $I4$ ) at ages of 1 Gyr and 5 Gyr. Error bars on these model derived properties only reflect the nominal uncertainty in the luminosity, i.e., due to the rms in parallax and bolometric corrections, at the given age. They do not include any potential systematic errors in bolometric corrections or the evolutionary model isochrones. Note that we assumed a spectral type of Y0 for CFBDSIR J145829+101343B here, solely for the purpose of computing  $m_{\text{bol}}$ .

<sup>a</sup>For Ross 458C ages of 150 Myr and 800 Myr were used instead of 1 Gyr and 5 Gyr, based on the age range determined by (21).

<sup>b</sup>For WD 0806-661B ages of 1.5 Gyr and 2.5 Gyr were used instead of 1 Gyr and 5 Gyr, based on the age range determined by (22).

Table S6. Mean Properties of Normal Late-T and Y dwarfs

| Spec. Type | $\log(L_{\text{bol}}/L_{\odot})$ | Cond ( $t = 1$ Gyr)     |                                     |                                     |                   |                  | Cond ( $t = 5$ Gyr)     |                                     |                                     |                   |                  |
|------------|----------------------------------|-------------------------|-------------------------------------|-------------------------------------|-------------------|------------------|-------------------------|-------------------------------------|-------------------------------------|-------------------|------------------|
|            |                                  | $T_{\text{eff}}$<br>(K) | $R_{\star}$<br>( $R_{\text{Jup}}$ ) | $M_{\star}$<br>( $M_{\text{Jup}}$ ) | $\log g$<br>(cgs) | D/D <sub>0</sub> | $T_{\text{eff}}$<br>(K) | $R_{\star}$<br>( $R_{\text{Jup}}$ ) | $M_{\star}$<br>( $M_{\text{Jup}}$ ) | $\log g$<br>(cgs) | D/D <sub>0</sub> |
| T8.0       | −5.72                            | 675                     | 0.982                               | 17                                  | 4.65              | 0.00             | 735                     | 0.826                               | 40                                  | 5.16              | 0.00             |
| T8.5       | −6.04                            | 550                     | 1.017                               | 12                                  | 4.44              | 0.29             | 600                     | 0.864                               | 31                                  | 5.00              | 0.00             |
| T9.0       | −6.15                            | 510                     | 1.019                               | 11                                  | 4.40              | 0.76             | 555                     | 0.879                               | 27                                  | 4.94              | 0.00             |
| T9.5       | −5.94                            | 585                     | 1.011                               | 13                                  | 4.49              | 0.27             | 640                     | 0.852                               | 33                                  | 5.05              | 0.00             |
| Y0.0       | −6.52                            | 410                     | 1.046                               | 8                                   | 4.23              | 1.00             | 440                     | 0.926                               | 18                                  | 4.72              | 0.00             |

Note. — Only “normal” objects are used for these weighted averages, i.e., excluding objects typed as peculiar (2MASS J0729−3954, BD+01 2920B, and WISEP J1405+5534), two Y0 dwarfs with very uncertain or preliminary distances (WISE J0359−5401 and WISE J1639−6847), and the young T8 dwarf Ross 458C. Averages are computed from the model-derived properties listed in Table S5, except for the deuterium abundance relative to the initial abundance (D/D<sub>0</sub>), which is only reported here. Effective temperatures are rounded to the nearest 5 K.